A SURVEY OF NUMERICAL SOLUTIONS TO THE COAGULATION EQUATION

MAN HOI LEE

Department of Physics, University of California, Santa Barbara, CA 93106, USA

E-mail: mhlee@europa.physics.ucsb.edu

ABSTRACT

We present the results of a systematic survey of numerical solutions to the coagulation equation for a rate coefficient of the form $A_{ij} \propto (i^\mu j^\nu + i^\nu j^\mu)$ and monodisperse initial conditions. The results confirm that there are three classes of rate coefficients with qualitatively different solutions. For $\nu \le 1$ and $\lambda = \mu + \nu \le 1$, the numerical solution evolves in an orderly fashion and tends toward a self-similar solution at large time t. The properties of the numerical solution in the scaling limit agree with the analytic predictions of van Dongen and Ernst. In particular, for the subset with $\mu > 0$ and $\lambda < 1$, we disagree with Krivitsky and find that the scaling function approaches the analytically predicted power-law behavior at small mass, but in a damped oscillatory fashion that was not known previously. For $\nu \le 1$ and $\lambda > 1$, the numerical solution tends toward a self-similar solution as t approaches a finite time t_0. The mass spectrum n_k develops at t_0 a power-law tail $n_k \propto k^{-\tau}$ at large mass that violates mass conservation, and runaway growth/gelation is expected to start at $t_{\text{crit}} = t_0$ in the limit the initial number of particles $n_0 \to \infty$. The exponent τ is in general less than the analytic prediction $(\lambda + 3)/2$, and $t_0 = K/[(\lambda - 1)n_0 A_{11}]$ with $K = 1$–2 if $\lambda \gtrsim 1.1$. For $\nu > 1$, the behaviors of the numerical solution are similar to those found in a previous paper by us. They strongly suggest that there are no self-consistent solutions at any time and that runaway growth is instantaneous in the limit $n_0 \to \infty$. They also indicate that the time t_{crit} for the onset of runaway growth decreases slowly toward zero with increasing n_0.

1. INTRODUCTION

Smoluchowski's coagulation equation is the mean-rate equation that describes the evolution of the mass spectrum of a collection of particles due to successive mergers. It is widely used for modeling growth in many fields of science. Examples include planetesimal accumulation, mergers in dense clusters of stars, coalescence of interstellar dust grains, and galaxy mergers in astrophysics, aerosol coalescence in atmospheric physics, colloids, and polymerization and gelation (see, e.g., Drake 1972, Ernst 1986, Jullien and Botet 1987, Lee 1993, 2000, and references therein).

If the masses of the particles are integral multiples of a minimum mass m_1, the coagulation equation is written in discrete form as

$$\frac{dn_k}{dt} = \frac{1}{2} \sum_{i+j=k} A_{ij} n_i n_j - n_k \sum_{i=1}^{\infty} A_{ki} n_i \tag{1}$$

where n_k is the number of particles of mass $m_k = km_1$ in a volume V and A_{ij} is the rate coefficient (or coagulation kernel) for mergers between particles of mass m_i and m_j.[1] In equation (1), it is assumed that the merging of two particles of mass m_i and m_j results in one particle of mass $m_i + m_j$. The coagulation equation can also be written in continuous form as

$$\frac{dn(m)}{dt} = \frac{1}{2} \int_0^m dm' \, A_{m',m-m'} n(m') n(m - m')$$
$$- n(m) \int_0^\infty dm' \, A_{m,m'} n(m') \tag{2}$$

where $n(m)dm$ is the number of particles of mass between m and $m+dm$ and $A_{m,m'}$ is the rate coefficient for mergers between particles of mass m and m'.

Examples of the rate coefficient A_{ij} as a function of m_i and m_j (or equivalently i and j) that arise in various problems can be found in the references cited above. Most rate coefficients used in the literature are homogeneous functions of degree λ, i.e., $A_{ai,aj} = a^\lambda A_{ij}$. The exponent λ specifies the mass dependence of the probability of merger for two particles of comparable mass ($i \sim j$). It is also useful to classify A_{ij} according to the exponents μ and ν for the merger between a light particle and a heavy particle: $A_{ij} \propto i^\mu j^\nu$ for $i \ll j$ and $\mu + \nu = \lambda$ (see, e.g., Ernst 1986). For example, $A_{ij} \propto i + j$ has $\mu = 0$, $\nu = 1$, and $\lambda = 1$.

For a few simple rate coefficients and monodisperse initial conditions (i.e., n_0 particles of mass m_1 at $t = 0$), there are exact analytic solutions to the discrete form

---

[1] We can interpret n_k as the concentration (i.e., the number of particles per unit volume) if we replace A_{ij} by $A'_{ij} = V A_{ij}$.

of the coagulation equation (Trubnikov 1971, Ernst 1986, and references therein). The analytic solutions for $A_{ij} \propto$ constant and $i + j$ show orderly evolution of a smooth mass spectrum at all times, and they agree with the results from Monte Carlo simulations of the merger process in the limit $n_0 \to \infty$ (with n_0/V fixed). These two cases are examples of orderly growth. The analytic solution for $A_{ij} \propto ij$ develops a power-law tail with $n_k \propto k^{-5/2}$ at large k as $t \uparrow t_0 = 1/(n_0 A_{11})$. This power-law tail violates mass conservation because it implies a nonzero mass flux to the infinite-mass bin. In this case, the results from Monte Carlo simulations in the limit $n_0 \to \infty$ agree with the solution to the coagulation equation at $t \leq t_0$, but they show a transition from a smooth mass spectrum to a smooth spectrum plus a massive runaway particle at $t = t_0$ (Spouge 1985, Wetherill 1990). The runaway particle (gel) acquires a mass much larger than that of the other particles (sol) in the system and becomes detached from the smooth mass spectrum of the rest of the particles at $t > t_0$. This phenomenon is known as runaway growth in the astrophysics literature, and the transition is considered to be the gelation transition in studies of polymerization and gelation.

For most rate coefficients, there are no exact analytic solutions to the coagulation equation. However, there are extensive analytic results on the asymptotic properties of the solutions for A_{ij} with $\nu \leq 1$ (see, e.g., review by Ernst 1986). It is important to note that some of these analytic results (such as the shape of the mass spectrum at small and large mass) are derived based on assumptions (such as self-similar evolution) that have not been verified. Nevertheless, the analytic results indicate that there are qualitatively two types of solutions to the coagulation equation if $\nu \leq 1$:

(1) if $\nu \leq 1$ and $\lambda \leq 1$, the solution shows orderly growth at all times;

(2) if $\nu \leq 1$ and $\lambda > 1$, the solution develops in a finite time t_0 a power-law tail at large mass that violates mass conservation.

For A_{ij} with essentially $\nu < 1$, it has been proved that a solution to the coagulation equation exists for all times (including $t > t_0$ if $\lambda > 1$) and that the coagulation equation is the limit of finite system (whether or not the runaway particle and the other particles are allowed to interact at $t > t_0$ if $\lambda > 1$) (Leyvraz and Tschudi 1981, Spouge 1985, Bak and Heilmann 1994, Jeon 1998). (For $\nu = 1$ and $\lambda > 1$, we have the example $A_{ij} \propto ij$, where the coagulation equation needs to be modified for $t > t_0$ if there is sol-gel interaction; Ziff *et al* 1983, Bak and Heilmann 1994.)

Several authors have investigated the properties of the solutions to the coagulation equation for A_{ij} with $\nu > 1$, using series expansion of the mass spectrum $n_k(t)$ about $t = 0$ and moments of the mass spectrum (McLeod 1962, Hendriks *et al* 1983, Ernst *et al* 1984, van Dongen 1987a). The results suggest that

(3) if $\nu > 1$, there are no self-consistent solutions that conserve mass at any time.

An alternative to the analytic approach is to solve the coagulation equation numerically. In Paper I (Lee 2000), a numerical code that can yield accurate solutions to the discrete form of the coagulation equation, equation (1), with a reasonable number of numerical mass bins was developed. The numerical code was used to study solutions to the coagulation equation for A_{ij} that are limiting cases for gravitational interaction. We considered geometric or gravitational focusing dominated cross-section, mass-independent or equipartition velocity dispersion, and the power-law index of the mass-radius relation $\beta = 1/3$ (for planetesimals) or $2/3$ (for stars). For the two cases with geometric cross-section and $\beta = 1/3$, which have $\nu \leq 1$ and $\lambda \leq 1$, the mass spectrum evolves in an orderly fashion and tends towards a self-similar solution at large time. For the remaining cases, which have $\nu > 1$, the numerical mass spectrum shows, after some evolution, an exponential drop in an intermediate mass range and a power-law tail of the form $n_k \propto k^{-\nu}$ (or $n(m) \propto m^{-\nu}$) at large mass. This mass spectrum is not self-consistent because the power-law tail implies a mass flux[2] and, if $1 < \nu \leq 2$, a cumulative mass that diverge with the maximum particle mass, $m_{\max}$, included in the computational grid. The time at which the power-law tail develops decreases toward zero as the numerical parameter $n_{\min}$ decreases (see Section 3 for the definition of $n_{\min}$). Thus the numerical results strongly suggest that there are no self-consistent solutions to the coagulation equation at any time if $\nu > 1$. We also considered a case with $\beta = 0$ as an example with $\nu \leq 1$ and $\lambda > 1$, and its mass spectrum develops a power-law tail that violates mass conservation in a finite time t_0. We discussed a simplified merger problem that illustrates the qualitative differences in the solutions to the coagulation equation for the three classes of A_{ij}. The results in Paper I (and the analytic results cited above) strongly suggest that there are two types of runaway growth. For A_{ij} with $\nu \leq 1$ and $\lambda > 1$, runaway growth starts at a finite time $t_{\mathrm{crit}} = t_0$, the time at which the coagulation equation solution begins to violate mass conservation, in the limit $n_0 \to \infty$. For A_{ij} with $\nu > 1$, runaway growth is instantaneous in the limit $n_0 \to \infty$, and there are indications (since decreasing $n_{\min}$

_____

[2] As we pointed out in Paper I, in these cases, a massive particle grows mainly by accumulating low-mass particles because of the much larger number of low-mass particles. So the growth rate of a massive particle is $\dot{m} = \int dm' A_{m,m'} n(m') m' \propto m^\nu$, since the integral is dominated by the range $m' \ll m$. Hence $n\dot{m}$ at the high-mass end of the mass spectrum is non-zero and independent of m if $n \propto m^{-\nu}$. However, we did not point out that the mass flux from particles of mass $m' \leq m$ to particles of mass $m' > m$ is $F_m \approx mn(m)\dot{m}(m) + \int_m^{m_{\max}} dm' n(m')\dot{m}(m')$. With $n\dot{m}$ independent of m, $F_m \approx n\dot{m}m_{\max}$, which is independent of m but increases with $m_{\max}$. We have verified this by an explicit evaluation of the mass flux (equation [12]) for the numerical solutions.

is similar to increasing n_0) that the time $t_{\rm crit}$, in units of $1/(n_0 A_{11})$, for the onset of runaway growth decreases slowly toward zero with increasing initial number of particles n_0. Recent Monte Carlo simulations have shown that the time for all particles to coalesce into a single particle decreases as a power of the logarithm of n_0 if $\nu > 1$ (Malyshkin and Goodman 2001; see also Spouge 1985, Jeon 1999).

The study in Paper I was focused on the rate coefficient for gravitational interaction, and the range of μ and ν studied was limited. In particular, μ was limited to 0 and $\pm 1/2$, and the region $\mu > 0$ and $\nu < 1$ was not studied at all. Other authors have obtained numerical solutions to the coagulation equation for rate coefficients that arise in specific problems. However, we are not aware of any study that has systematically surveyed the properties of numerical solutions as a function of μ and ν (and λ) and compared them to the analytic results on the asymptotic properties. For such a study, it is important that the numerical code used can follow the evolution of the mass spectrum accurately for a long time. After the computation for this paper was nearly complete, it came to our attention that Krivitsky (1995) has obtained numerical solutions to the continuous form of the coagulation equation, equation (2), for $A_{m,m'} \propto (mm')^{\lambda/2}$ (which has $\mu = \nu = \lambda/2$) and $A_{m,m'} \propto (m + m')^\nu$ (which has $\mu = 0$). For $A_{m,m'} \propto (mm')^{\lambda/2}$ with $\lambda \leq 1$, Krivitsky found that the numerical solutions are self-similar at large time, but that unlike the analytic result, the asymptotic behavior of the scaling function at small mass is not a power law. As we shall see, the latter result is incorrect because Krivitsky did not evolve the numerical solutions for a sufficiently long time to see the true asymptotic behavior at small mass. The scaling function does in fact approach the analytically predicted power law at small mass, but in a damped oscillatory fashion that was not known previously. It is unlikely that Krivitsky could have solved the coagulation equation accurately for the necessary amount of time because the numerical code used by Krivitsky does not conserve mass. For $A_{m,m'} \propto (m + m')^\nu$ with $\nu > 1$, Krivitsky found that the mass spectrum develops a slowly decreasing tail at very small time. Only the numerical solution for $\nu = 2$ was shown. Its evolution is qualitatively similar to that found in Paper I for $\nu > 1$, but it is not clear that the tail is power-law in nature because the maximum particle mass included in Krivitsky's computational grid is not large enough. It was also not demonstrated that the numerical solution is not sensitive to the other numerical parameters.

In this paper we present the results of a systematic survey of numerical solutions to the coagulation equation. The purpose of this survey is (1) to confirm that there are three classes of rate coefficients with qualitatively different solutions to the coagulation equation and that the boundaries of these three classes are as stated above; (2) to investigate, in the cases where self-consistent solutions exist, whether

the solutions approach self-similar solutions as $t \to \infty$ or $t \uparrow t_0$ and whether the scaling behaviors agree with the analytic results; (3) to study the dependence of t_0 on the exponents μ, ν, and λ for the runaway growth cases with $\nu \leq 1$ and $\lambda > 1$; and (4) to investigate whether the behaviors of the numerical solutions found in Paper I for the cases with $\nu > 1$ are valid in general. In Section 2 we describe the rate coefficient and the initial conditions used in this survey. In Section 3 we provide a brief summary of the numerical methods developed in Paper I for solving the coagulation equation and additional information on the accuracy of the numerical results. The results are presented in Section 4, and the conclusions are summarized in Section 5.

2. RATE COEFFICIENT AND INITIAL CONDITIONS

In this paper we consider a rate coefficient of the form

$$A_{ij} = \frac{1}{2} \left(i^\mu j^\nu + i^\nu j^\mu \right) \tag{3}$$

with $\mu \leq \nu$. Note that $A_{ai,aj} = a^{\mu+\nu} A_{ij}$ and $A_{ij} \propto i^\mu j^\nu$ for $i \ll j$, consistent with the definitions of the exponents μ, ν, and $\lambda = \mu + \nu$ in Section 1. Since the rate coefficient in equation (3) contains the exponents μ and ν as parameters explicitly, we can survey the entire (μ, ν) space by varying μ and ν. This rate coefficient includes $A_{ij} = (ij)^{\lambda/2}$ (for $\mu = \nu = \lambda/2$) and $A_{ij} = (i^\nu + j^\nu)/2$ (for $\mu = 0$), which have been used to model polymerization (e.g., Hendriks *et al* 1983), and the cases $(\mu, \nu) = (1, 4/3)$ and $(2, 2)$, which have been used to model planetesimal accumulation and stellar merger (Malyshkin and Goodman 2001). It also has the nice property that it includes the three cases with exact analytic solutions to the coagulation equation: $A_{ij} = 1$, $(i+j)/2$, and ij for $(\mu, \nu) = (0, 0)$, $(0, 1)$, and $(1, 1)$, respectively.

We have obtained numerical solutions to the discrete form of the coagulation equation for the cases shown in figure 1. The ranges of μ and ν considered contain most of the values encountered in practical applications (but usually for other forms of A_{ij}). The numerical solutions were computed for the monodisperse initial conditions with n_0 particles of mass m_1, i.e., $n_k(t = 0) = n_0 \delta_{k1}$, where δ_{k1} is the Kronecker delta. Hereafter, we adopt units such that $n_0 = 1$, $m_1 = 1$, and $A_{11} = 1$. With this set of units, $m_k = k$ and time is in units of $1/(n_0 A_{11})$, the timescale for every particle of mass m_1 to merge with another particle of mass m_1.

3. NUMERICAL METHODS

In Paper I we have developed a numerical code that can yield accurate solutions to the discrete form of the coagulation equation (equation [1]) with a reasonable

number of numerical mass bins. A detailed description of the code can be found in Paper I. In this section we provide a brief summary of the algorithm and its numerical parameters. We also provide additional information on the accuracy of the numerical results.

Our numerical code uses a combination of linearly and logarithmically spaced numerical mass bins. The first N_{bd} numerical mass bins are linearly spaced with $\tilde{m}_k = k$. They have boundaries $\tilde{m}_{k\pm1/2} = k \pm 1/2$ and width $\Delta\tilde{m}_k \equiv \tilde{m}_{k+1/2} - \tilde{m}_{k-1/2} = 1$. The next $N_{bd} \times N_{dec}$ numerical mass bins are logarithmically spaced, with N_{bd} bins per decade of mass; thus the kth mass is $\tilde{m}_k = (\tilde{m}_{k+1/2} + \tilde{m}_{k-1/2})/2$, with $\tilde{m}_{k+1/2}/\tilde{m}_{k-1/2} = 10^{1/N_{bd}}$. There are in total $N_{max} = (N_{dec} + 1)N_{bd}$ mass bins, and the mass of the most massive particles in the computational grid, m_{max}, is approximately $N_{bd}10^{N_{dec}}$. Initially, the number of "active" bins $N_{bin} \ll N_{max}$. At the end of each time step, N_{bin} is increased (if necessary) to include all bins with $N_k > n_{min}$, where N_k is the total number of particles in bin k and n_{min} is a numerical parameter; it is also increased if $N_{N_{bin}+1}$ becomes comparable to the power-law extrapolation from $N_{N_{bin}}$. Before N_{bin} reaches N_{max}, N_{max} (or equivalently m_{max}) has no effects on the numerical results. The numerical parameter n_{min} is specified in units of n_0 and, e.g., $n_{min} = 10^{-30}$ in units of n_0 is equivalent to $n_{min} = 1$ and $n_0 = 10^{30}$ in physical units. Thus the effect of the numerical parameter n_{min} is similar to not allowing fractionally occupied numerical mass bins to interact.

The fundamental quantity evolved by our numerical code is the total mass M_k in bin k. During a time step, the code calculates for each combination of i and j (with $i \leq j \leq N_{bin}$) the mass loss from bins i and j due to mergers between particles in those bins and distributes the total mass of the merger products among the mass bins. Thus the code conserves mass exactly. For $i \leq j \leq N_{bd}$, it is correct to assume that the merging particles have masses $\tilde{m}_i$ and $\tilde{m}_j$ and that the merger products have mass $\tilde{m}_i + \tilde{m}_j$. For $i \leq j$ and $j > N_{bd}$, we assume that the particles in bin i have mass $\tilde{m}_i$ (which is exact for $i \leq N_{bd}$) and that the mass distribution within bin j follows a power-law distribution:

$$\rho_j(m) = c_j(m/\tilde{m}_{j-1/2})^{q_j} \qquad \text{for } \tilde{m}_{j-1/2} < m \leq \tilde{m}_{j+1/2} \qquad (4)$$

where $\rho_j(m)dm$ is the total mass of particles with mass between m and $m+dm$. The merger products have masses between $\tilde{m}_i + \tilde{m}_{j-1/2}$ and $\tilde{m}_i + \tilde{m}_{j+1/2}$, and they are either added to a single bin k (if $\tilde{m}_{k-1/2} \leq \tilde{m}_i + \tilde{m}_{j-1/2}$ and $\tilde{m}_i + \tilde{m}_{j+1/2} \leq \tilde{m}_{k+1/2}$) or distributed between bins k and $k + 1$. In equation (4), the power-law index q_j is obtained from the masses in the adjacent bins,

$$q_j = \frac{\log\left(\frac{M_{j+1}}{\Delta\tilde{m}_{j+1}} \middle/ \frac{M_{j-1}}{\Delta\tilde{m}_{j-1}}\right)}{\log\left(\tilde{m}_{j+1}/\tilde{m}_{j-1}\right)} \qquad (5)$$

and the normalization constant c_j from the constraint

$$\int_{\tilde{m}_{j-1/2}}^{\tilde{m}_{j+1/2}} dm \, \rho_j(m) = M_j. \tag{6}$$

Our numerical code uses the second-order Runge-Kutta method with a variable time step. The time step is continuously adjusted so that the fractional change of each M_k per time step is less than δ_M and the mass loss from bin k does not exceed M_k.

In Paper I we have compared in detail the numerical solutions from our code to the exact analytic solutions for $A_{ij} = 1$, $(i+j)/2$, and ij, with the last case at $t < t_0$ only. The accuracy of the numerical solutions is extremely insensitive to δ_M and $n_{\min}$ and improves rapidly with increasing N_{bd}. Hereafter, unless stated otherwise, the numerical results were obtained using $\delta_M = 5\%$, $n_{\min} = 10^{-30}$ (in units of n_0), and $N_{bd} = 40$.

We report here several additional tests of our code. Ziff (1980) has constructed three forms of rate coefficients, with a parameter γ, for which a single moment $\mathcal{M}_\gamma(t) = \sum_{k=1}^{\infty} m_k^\gamma n_k(t)$ of the mass spectrum $n_k(t)$ can be calculated analytically. We have obtained numerical solutions for a few of these rate coefficients (including both orderly and runaway growth cases) and have confirmed that the numerical results for the moment $\mathcal{M}_\gamma(t)$ agree with the analytic results, with accuracy similar to what was found for the three cases with exact analytic solutions.

In Section 4.3 we shall be interested in extending the calculations for some of the runaway growth cases with $\nu \leq 1$ and $\lambda > 1$ to $t > t_0$. Therefore, another test that we have performed is to extend the comparison for the case $A_{ij} = ij$ to $t > t_0$. For $A_{ij} = ij$, the evolution of the mass spectrum at $t > t_0$ depends on whether or not the runaway particle (gel) and the other particles (sol) interact. The (unmodified) coagulation equation is valid if there is no sol-gel interaction, and it has an exact analytic solution with $n_k(t) \propto t^{-1} k^{-5/2}$ at large k for all $t > t_0$ (Leyvraz and Tschudi 1981, Ziff et al 1983). (The coagulation equation can be modified to take into account sol-gel interaction, and an exact analytic solution also exists for this modified coagulation equation; Ziff et al 1983.) Since our code does not take into account sol-gel interaction and does not allow merger products with masses greater than $m_{\max}$ to interact, we expect the numerical solution at $t > t_0$ to agree with the analytic solution to the unmodified coagulation equation, except for $m_k \sim m_{\max}$. We have integrated the case $A_{ij} = ij$ up to $t = 1.25$ and have found that the numerical solution at $t > t_0 = 1$ is in excellent agreement with the analytic solution for $m_k \lesssim 0.01 m_{\max}$.

A quantity that will be discussed extensively in Section 4 is the logarithmic slope $d\ln n/d\ln m$ of the mass spectrum. For the numerical results, we use

$$d\ln n/d\ln m \, (\tilde{m}_k) = q_k - 1 \tag{7}$$

where q_k is defined in equation (5). Equation (7) is consistent with the power-law approximation used by the code since under this approximation the number distribution of particles within the numerical mass bin k is $n_k(m) = \rho_k(m)/m \propto m^{q_k-1}$.

To determine the accuracy of the numerical results for $d\ln n/d\ln m$, we compare the numerical and analytic results for the three cases with exact analytic solutions. The analytic solutions are of the form $n \propto m^{-\tau}\exp[-b(t)\,m]$ or $d\ln n/d\ln m = -\tau - b(t)\,m$ for $m \gg 1$, where $\tau = 0$, $3/2$, and $5/2$ for $A_{ij} = 1$, $(i+j)/2$, and ij, respectively. Thus $n \propto m^{-\tau}$ or $d\ln n/d\ln m = -\tau$ for $1 \ll m \ll m_*$ when the characteristic mass $m_*(t)$ defined in equation (9) is large. In figure 2(a) we show for each case the numerical and analytic $d\ln n/d\ln m$ at $m \lesssim m_*(t)$ at a given time. As we noted in Paper I, there is a small lag in the evolution of the numerical solutions for $A_{ij} = (i+j)/2$ and ij. Therefore, in these cases, the numerical results are compared to the analytic results at a slightly earlier time. There are fluctuations in the numerical results in the first decade of the logarithmically spaced mass bins ($1 \lesssim m/N_{bd} \lesssim 10$) due to the discreteness of the mass bins, but the fluctuations are $\lesssim 0.015$. The numerical results are much smoother and much more accurate outside this mass range. We can see from figure 2(a) that τ can be determined from the numerical results at $1 \ll m \ll m_*$ to better than ± 0.001.

Figure 2(b) is similar to figure 2(a), but it shows the mass range $m \gtrsim m_*(t)$. The differences between the analytic results, which decrease linearly with mass, and the numerical results are small, but there is a small curvature in the numerical results, and the numerical results become increasingly higher than the analytic results with increasing mass. (This is consistent with the observation in Paper I that the numerical solutions show a slightly slower exponential decay at the high-mass end of the mass spectrum.) As a result, if we fit the numerical results near $d\ln n/d\ln m = -20$ (or -30) to a straight line $d\ln n/d\ln m = -\theta - bm$, the resulting values for θ are greater than the correct values (which are τ as given above) by 0.13–0.15 (or 0.29–0.36). This is the accuracy to which we can check whether a numerical solution is consistent with $d\ln n/d\ln m = -\theta - bm$ and a given θ at $m \gg m_*$.

In Paper I we have discussed our numerical code in the context of numerical codes in the astrophysics literature. Other recent numerical codes include those by Krivitsky (1995), Hill and Ng (1996), and Tzivion et al (1999). As we mentioned in Section 1, the numerical code used by Krivitsky does not conserve mass and would have difficulty following the evolution of the mass spectrum accurately for a long time. The numerical code described by Hill and Ng conserves mass but uses a relatively simple algorithm for distributing merger products. We had in fact tried a similar algorithm for distributing merger products (Quinlan and Shapiro 1989) before we developed the algorithm based on the power-law approximation

and had found that the high-mass end of the mass spectrum converges very slowly with increasing grid resolution (N_{bd}) if the rate coefficient increases steeply with the mass of the particles (i.e., if ν and/or λ is large). Tzivion *et al* have developed a mass-conserving numerical code that evolves separately the total number (N_k) and mass (M_k) of particles in a numerical mass bin k. The numerical solutions obtained using this code appear to converge rapidly with increasing grid resolution for the case $A_{m,m'} \propto m + m'$, but there was no demonstration that this is also true for rate coefficients with steeper mass dependence.

4. RESULTS

In this section we present the numerical solutions to the discrete form of the coagulation equation for the rate coefficient and initial conditions described in Section 2 (see also figure 1). For the cases with $\nu \leq 1$ (Sections 4.1–4.3), whenever possible, we compare the properties of the numerical solutions to the predictions from self-similar analysis. Hereafter, unless otherwise stated, the self-similar analysis results cited can be found in van Dongen and Ernst (1985a, 1988).

4.1. Orderly Growth Cases with $\nu \leq 1$ and $\lambda < 1$

An example of the numerical results for the mass spectrum evolution for $\nu \leq 1$ and $\lambda < 1$ is shown in figure 3.[3] In this and all other cases with $\nu \leq 1$ and $\lambda < 1$, the mass spectrum evolves in an orderly fashion. For these cases, we stopped the numerical integrations when the asymptotic behaviors of the solutions were clear and before N_{bin} reached N_{max}.

For orderly growth with $\nu \leq 1$ and $\lambda < 1$, self-similar analysis predicts that self-similar solutions have the form

$$n_k(t) = m_*(t)^{-2} \varphi[m_k/m_*(t)] \tag{8}$$

where $\varphi(x)$ is a scaling function, and the characteristic mass $m_*(t)$ scales as $t^{1/(1-\lambda)}$. Different definitions of $m_*(t)$, which correspond to different scales for $x = m_k/m_*(t)$ and $\varphi(x)$, can be used. We adopt

$$m_*(t) = \mathcal{M}_3(t)/\mathcal{M}_2(t) \tag{9}$$

where $\mathcal{M}_\ell(t) \equiv \sum_{k=1}^{\infty} m_k^\ell n_k(t)$ is the ℓth moment of the mass spectrum. This choice of m_* is convenient because it can also be used for runaway growth with $\nu \leq 1$ and $\lambda > 1$ (Section 4.3).

---

[3] In figure 3 and all subsequent figures, the numerical mass spectrum plotted is $n(\tilde{m}_k) = N_k$ for $k \leq N_{bd}$ and $n(\tilde{m}_k) = n_k(\tilde{m}_k)$ for $k > N_{bd}$.

In all cases, the numerical solution tends toward a self-similar solution of the form (8) at large t. This is illustrated in figure 4, where we plot the numerical solution at three different times in the form of $\log m^2 n$ as a function of $\log m/m_*$ for the case shown in figure 3. In the scaling limit (8), $m^2 n = x^2 \varphi(x)$. We have evaluated the exponent $z(t_i) = \ln[m_*(t_{i+1})/m_*(t_{i-1})]/\ln(t_{i+1}/t_{i-1})$ from the numerical results for $m_*(t)$ at output times t_{i-1}, t_i, and t_{i+1} for all cases with $\nu \leq 1$ and $\lambda < 1$. In all but two cases, the exponent z at large t agrees with $1/(1-\lambda)$ to better than one part in 1.5×10^3. For the two cases with $(\mu, \nu) = (1/6, 2/3)$ and $(1/3, 1/2)$, the agreement between the numerical results at the end of the numerical runs, $z = 5.985$ and 5.963, and the analytic result, $1/(1-\lambda) = 6$, is slightly worse, but the numerically determined exponents are still slowly increasing with time at the end of the numerical runs, indicating that the numerical results have not completely reached the asymptotic regime.

Figure 5 shows the numerical results for the scaling function $\varphi(x)$ for all cases with $\nu \leq 1$ and $\lambda < 1$. The location of the peak of $x^2 \varphi$ is not very sensitive to μ or ν, and it is at $x = 0.33$–0.71. Self-similar analysis predicts that the scaling function $\varphi(x)$ decays exponentially at large x. For $\nu < 1$, $\varphi(x) \propto x^{-\theta} \exp(-bx)$ or $d\ln \varphi/d\ln x = -\theta - bx$, with $\theta = \lambda$, at large x. The detailed behavior of $\varphi(x)$ at large x for $\nu = 1$ depends on the specific form of A_{ij}. For A_{ij} in equation (3) with $\nu = 1$, the large-x behavior of $\varphi(x)$ is similar to that for $\nu < 1$, but $\theta = (\mu + 3)/2$ if $-1 \leq \mu < 0$ (van Dongen 1987b; see also Ernst *et al* 1984). In all cases, the numerical $\varphi(x)$ decays exponentially at large x, and $d\ln \varphi/d\ln x$ at large x is consistent with the analytic result (see Section 3 for a discussion of the accuracy of the numerical results at large x).

The behavior of the scaling function $\varphi(x)$ at small x is qualitatively different for $\mu < 0$, $\mu = 0$, and $\mu > 0$. For the cases with $\mu < 0$ (figure 5(a)), $\varphi(x)$ also decays exponentially at small x, because light particles are rapidly accreted by heavy particles. Self-similar analysis predicts that $\varphi(x) \propto x^{-a} \exp(bx^\mu/\mu)$ or $d\ln \varphi/d\ln x = -a + bx^\mu$ at small x, where a and b are constants that depend on the specific form of A_{ij}. For A_{ij} in equation (3), $a = 2$ if $\nu > 0$ and $a = 1$ if $\nu = 0$. In figure 6, we plot the numerical results for $d\ln \varphi/d\ln x$ as a function of x^μ for the cases with $\mu = -1/6$ to show that the numerical results indeed have the form $d\ln \varphi/d\ln x = -a + bx^\mu$ at large x^μ (or small x). Furthermore, in all cases with $\mu < 0$, the value of a from least-squares fit is in agreement with the analytic result to better than ± 0.004.

For the cases with $\mu = 0$, i.e., $A_{ij} = (i^\nu + j^\nu)/2$, the scaling function shows a power-law behavior $\varphi(x) \propto x^{-\tau}$ at small x (figure 5(b)). The numerical results for the exponent τ are 0.000, 1.001, 1.033, 1.109, 1.216, 1.347, and 1.500 for $\nu = 0$, 1/6, 1/3, 1/2, 2/3, 5/6, and 1, respectively. Self-similar analysis gives $\tau = 2 - p_\lambda/w$,

where p_λ and w depend on the specific form of A_{ij}. van Dongen and Ernst (1985b) have used this expression to derive analytic lower and upper bounds on τ for $A_{ij} = (i^\nu + j^\nu)/2$. Our numerical results are consistent with these bounds. Note that the exponent τ is discontinuous at $\nu = 0$: τ decreases from 1.5 at $\nu = 1$ to 1 as $\nu \downarrow 0$, but $\tau = 0$ at $\nu = 0$ (recall that the $\nu = 0$ and $\nu = 1$ cases have exact analytic solutions). In contrast, for $A_{ij} \propto (i + j)^\nu$ (which also has $\mu = 0$), the exponent τ decreases smoothly from 1.5 at $\nu = 1$ to 0 at $\nu = 0$ (van Dongen and Ernst 1985c, Krivitsky 1995).

For the cases with $\mu > 0$ (figure 5(c)), the scaling function $\varphi(x)$ oscillates around a power law at small x, with the fractional amplitude of the oscillation decreasing as $x \to 0$. This damped oscillatory approach to a power law is shown more clearly in figure 7, where we plot the logarithmic slope $d\ln\varphi/d\ln x$ as a function of $\log x$ for the cases with $\mu = 1/6$. In all cases, the logarithmic slope tends to a constant value as $x \to 0$, and the asymptotic value is consistent with the leading small-x behavior predicted by self-similar analysis: $\varphi(x) \propto x^{-(1+\lambda)}$ or $d\ln\varphi/d\ln x = -(1+\lambda)$. The oscillation appears to be periodic in the variable $\ln x$, but it is difficult to determine this accurately because of the limited number of cycles seen in our numerical results.

The damped oscillatory behavior at small x for $\mu > 0$ and $\lambda < 1$ was not known previously. In their self-similar analysis, van Dongen and Ernst (1988) were unable to find higher-order corrections to the leading small-x behavior of $\varphi(x)$ for $\mu > 0$ and $\lambda < 1$, and they raised the possibility that physically acceptable self-similar solutions may not exist. As we have just shown, there are indeed physically acceptable self-similar solutions, and they are reached from monodisperse initial conditions. Based on our numerical results, we suggest that the leading small-x behavior and the first correction could be of the form $\varphi(x) \propto x^{-(1+\lambda)}[1 + f(x)\cos(B\ln x + C)]$, where $f(x)$ is an increasing function of x, possibly Ax^α with $\alpha > 0$. The failure to find the first correction in the self-similar analysis is probably due to the unusual form of this correction.

As we mentioned in Section 1, Krivitsky (1995) has obtained numerical solutions to the continuous form of the coagulation equation for $A_{m,m'} \propto (mm')^{\lambda/2}$ with $\lambda \leq 1$. Krivitsky concluded that the numerical solutions are self-similar at large time but that the asymptotic behavior at small mass is not a power law. The latter conclusion is different from ours and, we believe, incorrect. We can understand why Krivitsky reached this conclusion by examining figure 5(b) of Krivitsky (1995), where the numerical results for $d\ln n/d\ln m$ are shown for the case $\lambda = 0.4$. By the last time shown, the numerical results have converged to a self-similar form for $x \gtrsim 10^{-4}$, and the logarithmic slope is indeed decreasing with decreasing x over the range $10^{-4} \lesssim x \lesssim 10^{-1}$. However, as we can see from our figure 7, over this

range in x, $d \ln \varphi / d \ln x$ is in fact decreasing from a maximum to a minimum in its oscillatory approach to a constant value. Therefore, the incorrect conclusion was reached because Krivitsky did not evolve the numerical solutions for a sufficiently long time to see the true asymptotic behavior at small mass.

4.2. Orderly Growth Cases with $\nu \leq 1$ and $\lambda = 1$

On the borderline $\lambda = 1$ and $\nu \leq 1$, the numerical mass spectrum evolves in an orderly fashion, but with the characteristic mass $m_*(t)$ increasing exponentially with time. For these cases, we set $N_{\mathrm{dec}} = 19$ and stopped the numerical integrations as soon as N_{bin} reached N_{max}, i.e., when the mass spectra extended over 20 decades in mass.

We distinguish the cases with $\mu = 0$ and $\mu > 0$. As we discussed above, the case $\mu = 0$ is $A_{ij} = (i + j)/2$ with exact analytic solution, and the numerical solution for this case is in excellent agreement with the analytic solution (see Section 3 and figures 2 and 5(b)). The mass spectrum tends toward a self-similar solution of the form (8) at large t, with $m_*(t) \propto e^t$ (see figure 8), and the scaling function $\varphi(x) \propto x^{-3/2}$ at small x and $\propto x^{-\theta} \exp(-bx)$ with $\theta = (\mu + 3)/2 = 3/2$ at large x.

For $\mu > 0$, van Dongen and Ernst (1988) have derived a modified self-similar solution:

$$n_k(t) = (m_*^2 \ln m_*)^{-1} \varphi(m_k/m_*) \tag{10}$$

where $(\ln m_*)^2 = a + bt$ and a and b are constants. The scaling function $\varphi(x)$ is predicted to scale as x^{-2} at small x and $x^{-1} \exp(-bx)$ at large x.

The numerical results for $m_*(t)$ for the three cases with $\mu > 0$ (and also the case $\mu = 0$) are shown in figure 8. In each case, we have fitted the numerical results at the last two output times to $\ln m_* = a + bt$ and $(\ln m_*)^2 = a + bt$, and they are shown as dotted and solid lines, respectively. For $(\mu, \nu) = (1/2, 1/2)$, $(\ln m_*)^2 = a + bt$ provides a reasonably good fit to the numerical results at large t. For $(\mu, \nu) = (1/3, 2/3)$ and, in particular, $(1/6, 5/6)$, the numerical results at large t show deviations from $(\ln m_*)^2 = a + bt$. The deviations in the last two cases are probably due to the numerical results not having completely reached the asymptotic regime, but we cannot rule out the possibility that the asymptotic behavior is different from the analytic prediction.

If a numerical solution approaches the self-similar solution (10), we expect $m^2 n \ln m_* \rightarrow x^2 \varphi(x)$ and $d \ln n / d \ln m \rightarrow d \ln \varphi / d \ln x$. In figure 9 we show $d \ln n / d \ln m$ as a function of $\log m/m_*$ at three different times for all cases with $\mu > 0$ and $\lambda = 1$. For $(\mu, \nu) = (1/2, 1/2)$, $d \ln n / d \ln m$ has converged to $d \ln \varphi / d \ln x$ at $x = m/m_* \gtrsim 10^{-5}$, but the convergence at $x \lesssim 10^{-5}$ is very slow and is not complete by the end of the numerical run. The range of x over which $d \ln n / d \ln m$

has converged by the end of the numerical run is wider for smaller μ. (A similar analysis of $m^2 n \ln m_*$ reveals a small increase in the normalization of $m^2 n \ln m_*$ with time in the range of x where $d \ln n / d \ln m$ has converged. This increase is more pronounced for smaller μ and is probably due to m_* not having completely reached the asymptotic regime.) For $(\mu, \nu) = (1/6, 5/6)$, it is reasonably clear that $d \ln \varphi / d \ln x \to -2$ in the small-x limit, consistent with the analytic prediction. For $(\mu, \nu) = (1/3, 2/3)$ and $(1/2, 1/2)$, the small-x behaviors are less certain because of the slow convergence at small x, but they also appear to be consistent with the analytic prediction. Finally, in all three cases, the large-x behavior of the numerical $d \ln \varphi / d \ln x$ is consistent with the analytic prediction that $d \ln \varphi / d \ln x = -1 - bx$.

4.3. Runaway Growth Cases with $\nu \leq 1$ and $\lambda > 1$

In all cases with $\nu \leq 1$ and $\lambda > 1$, the numerical mass spectrum develops in a finite time t_0 a power-law tail, $n_k \propto k^{-\tau}$, at large mass that violates mass conservation, and runaway growth is expected to start at $t_{\mathrm{crit}} = t_0$ in the limit $n_0 \to \infty$. For most cases with $\nu \leq 1$ and $\lambda > 1$, we stopped the numerical integrations as soon as N_{bin} reached N_{max} and the mass spectra extended over 20 decades in mass; so the numerical solutions approach very close to but do not exceed t_0. To study the transition at $t = t_0$, we extended the integrations for the cases $(\mu, \nu) = (1/3, 1)$ and $(2/3, 2/3)$ to $t > t_0$. Figure 10 shows the numerical results for the mass spectrum evolution for the case $(\mu, \nu) = (1/3, 1)$ at $t \leq t_0$ (solid lines) and $t > t_0$ (dashed lines).

For runaway growth with $\nu \leq 1$ and $\lambda > 1$, self-similar analysis predicts that self-similar solutions close to but before t_0 have the form

$$n_k(t) = m_*(t)^{-\tau} \varphi[m_k / m_*(t)] \tag{11}$$

where the scaling function $\varphi(x) \propto x^{-\tau}$ at small x, the characteristic mass $m_*(t)$ diverges as $(t_0 - t)^{-1/\sigma}$, and $\sigma = \lambda + 1 - \tau$. With $m_*(t)$ diverging at t_0, the self-similar solution (11) has $n_k(t_0) \propto k^{-\tau}$ at large k. In all cases, the numerical solution tends toward a self-similar solution of the form (11) as $t \uparrow t_0$, and the numerical $\varphi(x)$ is indeed a power law at small x. This is illustrated in figure 11, where we plot the numerical solution at three different times $(< t_0)$ in the form of $\log(m^2 n \, m_*^{\tau-2})$ as a function of $\log m/m_*$ for the case shown in figure 10, with the exponent τ determined from the numerical solution itself (see table 1 and discussion below). In the scaling limit (11), $m^2 n \, m_*^{\tau-2} = x^2 \varphi(x)$.

Despite the change in the form of the self-similar solution, the analytic predictions for the large-x behavior of $\varphi(x)$ are similar to those for orderly growth in Sections 4.1–4.2: $\varphi(x) \propto x^{-\theta} \exp(-bx)$ or $d \ln \varphi / d \ln x = -\theta - bx$, where $\theta = \lambda$

if $\nu < 1$, $\theta = (\mu + 3)/2$ if $\nu = 1$ and $0 < \mu < 1$, and $\theta = 5/2$ if $\nu = \mu = 1$. In all cases, the numerical $\varphi(x)$ decays exponentially at large x, and $d \ln \varphi / d \ln x$ at large x is consistent with the analytic result.

The analytic predictions for the exponents τ and σ are $\tau = (\lambda + 3)/2$ and $\sigma = \lambda + 1 - \tau = (\lambda - 1)/2$ (Hendriks *et al* 1983, van Dongen and Ernst 1985a, 1988). For comparison, we have determined τ and σ from the numerical results for $d \ln \varphi / d \ln x$ and $m_*(t)$, respectively. In figure 12 we show the numerical results for $d \ln \varphi / d \ln x$ for the cases with $\lambda = 4/3$. The numerical results clearly converge to constant values at small x. The constant asymptotic values are consistent with $\varphi(x) \propto x^{-\tau}$ or $d \ln \varphi / d \ln x = -\tau$ at small x and directly yield the values of τ. It is also clear from figure 12 that the asymptotic values and hence τ for these cases with the same $\lambda(= 4/3)$ are different from each other and from the analytic prediction that $d \ln \varphi / d \ln x = -\tau = -(\lambda + 3)/2 = -13/6$ (dashed line in figure 12). The numerical results for the exponent τ for all cases with $\nu \leq 1$ and $\lambda > 1$ are listed in table 1. The only case where the exponent τ agrees with the analytic prediction $(\lambda + 3)/2$ is the case $\nu = \mu = 1$ (i.e., the case $A_{ij} = ij$ with exact analytic solution). In all other cases, the exponent τ is less than $(\lambda + 3)/2$. For a given λ, the deviation of τ from $(\lambda + 3)/2$ is largest for $\nu = 1$ and smallest for $\nu = \mu$.

To determine the exponent σ, we fit the numerical results for $m_*(t)$ at output times t_{i-1}, t_i, and t_{i+1} to $m_*(t) = C(t_0' - t)^{-1/\sigma'}$ to obtain $C(t_i)$, $t_0'(t_i)$, and $\sigma'(t_i)$. In most cases, $\sigma'(t)$ has converged to a constant value by the end of the numerical run and directly yields σ. In the remaining cases, we extrapolated $\sigma'(t)$ to the limit $m_*(t) \to \infty$ to obtain σ, but the difference between $\sigma'(t)$ at the end of the numerical run and σ is ≤ 0.002. The numerical results for the exponent σ are listed in table 1, together with $\lambda + 1 - \tau$. Except for the case $\nu = \mu = 1$, the exponent σ is greater than the analytic prediction $(\lambda - 1)/2$. For a given λ, the deviation of σ from $(\lambda - 1)/2$ is largest for $\nu = 1$ and smallest for $\nu = \mu$. We note that the numerical results for σ and τ are consistent with one another in that they satisfy the relation $\sigma = \lambda + 1 - \tau$ for self-similar solutions of the form (11) to within ± 0.001.

The procedure described above for determining the exponent σ also yields the time t_0. The numerical results for t_0, in units of $1/(n_0 A_{11})$, are listed in table 1. Since we expect $t_0 \sim 1/[(\lambda - 1)n_0 A_{11}]$ (see Paper I), it is convenient to parameterize t_0 as $t_0 = K/[(\lambda - 1)n_0 A_{11}]$. The parameter K is shown in figure 13. We find that $K = 1$–2 if $\lambda \gtrsim 1.1$ and that, for a given λ, K is smallest for $\nu = 1$ and largest for $\nu = \mu$. For $\nu = 1$, the parameter K shows a maximum at $\lambda \approx 1.3$. For $\nu = \mu$, K increases monotonically with decreasing λ, but it is unclear whether K approaches a constant value or diverges as $\lambda \to 1$. Finally, we note that the numerical results for t_0 are consistent with the bound $t_0 \geq 1/[(\lambda - 1)n_0 A_{11}]$ for A_{ij} in equation (3) and monodisperse initial conditions and the stronger bound $t_0 \geq 1/[(2^{\lambda-1} - 1)n_0 A_{11}]$

for $\nu = \mu$, derived analytically by Hendriks *et al* (1983).

We have found that the exponents τ and σ are in general different from the analytic predictions. Since the analytic prediction for σ follows from that for τ and the relation $\sigma = \lambda + 1 - \tau$ for self-similar solutions of the form (11), and the numerical results for σ and τ satisfy this relation, we have essentially a discrepancy in the exponent τ. Let us examine the derivation of the analytic prediction for τ, which can be summarized as follows (see Hendriks *et al* 1983, van Dongen and Ernst 1985a, 1988 for details). The mass flux from particles of mass $m_i \leq m_k$ to particles of mass $m_i > m_k$ is

$$F_k(t) = \sum_{i=1}^{k} \sum_{j=k+1-i}^{\infty} m_i A_{ij} n_i(t) n_j(t). \tag{12}$$

It is assumed that solutions to the coagulation equation at $t > t_0$ violate mass conservation by having a non-zero and finite mass flux to the infinite-mass bin (i.e., in the limit $k \to \infty$), which is possible only if the mass spectrum at $t > t_0$ is of the form $n_k(t) \propto k^{-\tau'}$ at large k. With $n_k(t) \propto k^{-\tau'}$ at large k, the mass flux $F_k(t) \propto k^{\lambda+3-2\tau'}$ at large k. Thus $\tau' = (\lambda + 3)/2$ if the mass flux $F_k(t)$ is required to be non-zero and finite in the limit $k \to \infty$. Since the self-similar solution (11) has $n_k(t_0) \propto k^{-\tau}$ at large k, $\tau = \tau' = (\lambda + 3)/2$ if we assume that the large-k behavior at $t > t_0$ is also valid at $t = t_0$. It should be noted that the arguments leading to $\tau = (\lambda + 3)/2$ are not rigorous. In particular, as van Dongen and Ernst (1988) pointed out, one cannot exclude the possibility that the mass flux diverges at one instant of time, i.e., t_0. We have found that $\tau < (\lambda + 3)/2$ in general. This implies that the mass flux F_k at t_0, which is $\propto k^{\lambda+3-2\tau}$ at large k, diverges as $k \to \infty$. Thus the numerical solutions violate mass conservation at t_0 by having a diverging mass flux to the infinite-mass bin.

Since the mass flux cannot diverge for all times $t > t_0$, do the solutions at $t > t_0$ have the form $n_k(t) \propto k^{-(\lambda+3)/2}$ at large k for non-zero and finite mass flux to the infinite-mass bin? If so, how can this large-k behavior at $t > t_0$ be reconciled with that at $t = t_0$? To answer these questions, we have extended the numerical integrations for the cases $(\mu, \nu) = (1/3, 1)$ and $(2/3, 2/3)$ to $t > t_0$. The results for the mass spectrum evolution at $t > t_0$ for the case $(\mu, \nu) = (1/3, 1)$ are shown as dashed lines in figure 10. As in the test case $A_{ij} = ij$ discussed in Section 3, the numerical solution at $m_k \sim m_{\max}$ is affected by the finite value of the maximum particle mass, $m_{\max}$, in the computational grid. Otherwise, the mass spectrum at $t > t_0$ is indeed of the form $n_k(t) \propto k^{-(\lambda+3)/2}$ at large k, with the value of the exponent confirmed by an analysis of the logarithmic slope. Note, however, that the range of k where $n_k(t) \propto k^{-(\lambda+3)/2}$ shrinks toward infinity as $t \downarrow t_0$. The numerical solution for the case $(\mu, \nu) = (2/3, 2/3)$ shows the same large-k behaviors

at $t > t_0$. Therefore, we conclude that the transition at $t = t_0$ is accomplished as follows. As $t \uparrow t_0$, the solution tends toward a self-similar solution of the form (11), with $n_k(t) \propto k^{-\tau}$ for $1 \ll m_k \ll m_*(t)$, $\tau < (\lambda + 3)/2$ in general, and $m_*(t) \to \infty$. As $t \downarrow t_0$, $n_k(t) \propto k^{-(\lambda+3)/2}$ for $m_k \gg m'_*(t)$ and $m'_*(t) \to \infty$.

4.4. *Runaway Growth Cases with $\nu > 1$*

Examples of the numerical results for the mass spectrum evolution with $n_{\min} = 10^{-30}$ (solid lines) and 10^{-35} (dotted lines) for $\nu > 1$ are shown in the lower panels of figure 14. In all cases with $\nu = 2$ and $3/2$ and the three cases with $\nu = 7/6$ and $\mu \leq 0$ (see, e.g., figure 14(a)), the behaviors of the numerical solutions for both $n_{\min} = 10^{-30}$ and 10^{-35} are qualitatively similar to those found in Paper I for other forms of A_{ij} with $\nu > 1$. In the early stages, the mass spectrum appears to decay exponentially at large mass. After some evolution, the mass spectrum shows an exponential drop in an intermediate mass range and a power-law tail of the form $n_k \propto k^{-\nu}$ (or $n \propto m^{-\nu}$) at large mass. For the three cases with $\nu = 7/6$ and $\mu \geq 1/3$, the numerical solutions with $n_{\min} = 10^{-30}$ do not develop the $m^{-\nu}$ tail when N_{bin} reaches $N_{\max}$ (see, e.g., figure 14(b)), and their behaviors are qualitatively similar to those for the runaway growth cases with $\nu \leq 1$ and $\lambda > 1$ (Section 4.3; figure 10). When $n_{\min}$ is decreased to 10^{-35}, the $\mu = 1/3$ case does develop an $m^{-\nu}$ tail when N_{bin} reaches $N_{\max}$ (figure 14(b)), but the other two cases do not. It is not feasible to compute solutions for much smaller $n_{\min}$, but we strongly suspect that the remaining two cases would develop the $m^{-\nu}$ tail for sufficiently small $n_{\min}$.

The fact that the tail at large mass is of the form $n \propto m^{-\nu}$ or $d \ln n / d \ln m = -\nu$ is illustrated in the upper panels of figure 14, where we plot the numerical results for $d \ln n / d \ln m$ at the specified times, just after the formation of the tail for the runs with $n_{\min} = 10^{-35}$. As found in Paper I, the time at which the power-law tail develops decreases slowly toward zero as $n_{\min}$ decreases (lower panels of figure 14). We do not repeat the demonstrations here, but it was shown in Paper I that numerical solutions with different maximum particle mass, $m_{\max}$, included in the computational grid are identical in the overlapping mass range and that the power-law tail simply extends to larger particle mass m when $m_{\max}$ is increased. (It was also shown that the numerical solutions converge by $N_{bd} = 40$ and $\delta_M = 5\%$.) Therefore, in the limit $n_{\min} \to 0$ and $m_{\max} \to \infty$, the numerical solutions for all cases with $\nu > 1$ (with the possible exception of the cases with $\nu = 7/6$ and $\mu > 1/3$) should develop in an infinitesimal time power-law tails of the form $n \propto m^{-\nu}$ that extend to arbitrarily large $m_{\max}$. However, this mass spectrum is not self-consistent because the power-law tail implies a mass flux and, if $1 < \nu \leq 2$, a cumulative mass that diverge with $m_{\max}$ (see footnote 2 and Paper I). Thus, as in Paper I, the numerical results strongly suggest that there are no self-consistent solutions to the

coagulation equation at any time if $\nu > 1$. Furthermore, since the formation of the power-law tail in the coagulation equation solution with finite $n_{\min}$ probably corresponds to the onset of runaway growth in Monte Carlo simulations with finite n_0 (see Paper I) and decreasing $n_{\min}$ is equivalent to increasing n_0 (see Section 3), the time t_{crit} for the onset of runaway growth for $\nu > 1$ should decrease slowly toward zero with increasing n_0.

5. CONCLUSIONS

We have conducted a systematic survey of numerical solutions to the coagulation equation (1) for a rate coefficient of the form $A_{ij} \propto (i^\mu j^\nu + i^\nu j^\mu)$ and monodisperse initial conditions. The numerical results confirmed that there are three classes of rate coefficients with qualitatively different solutions to the coagulation equation.

For $\nu \leq 1$ and $\lambda = \mu + \nu < 1$ (Section 4.1), the numerical solution evolves in an orderly fashion and tends toward a self-similar solution of the form (8) at large time t. The time dependence of the characteristic mass $m_*(t)$ at large t and the behaviors of the scaling function $\varphi(x)$ at small and large $x = m_k/m_*(t)$ agree with the analytic predictions of van Dongen and Ernst (1985a, 1988). In particular, for the subset of cases with $\mu > 0$, we disagreed with the earlier numerical study by Krivitsky (1995) and found that $\varphi(x)$ does in fact approach the analytically predicted power-law behavior $\varphi(x) \propto x^{-(1+\lambda)}$ at small x, but in a damped oscillatory fashion that was not known previously (figure 7). For $\mu = 0$, we determined the exponent τ of the power-law behavior $\varphi(x) \propto x^{-\tau}$ at small x.

On the borderline $\nu \leq 1$ and $\lambda = 1$ (Section 4.2), the numerical solution evolves in an orderly fashion. For $\mu = 0$, i.e., $A_{ij} \propto i + j$, the numerical solution is in excellent agreement with the exact analytic solution and tends toward a self-similar solution of the form (8) at large t. For $\mu > 0$, the numerical solution appears to tend toward a self-similar solution of the form (10), but we had limited success in comparing the behaviors of $m_*(t)$ and $\varphi(x)$ at small x to the analytic predictions because the convergence to the self-similar solution is very slow.

For $\nu \leq 1$ and $\lambda > 1$ (Section 4.3), the numerical mass spectrum n_k develops in a finite time t_0 a power-law tail, $n_k \propto k^{-\tau}$, at large k that violates mass conservation, and runaway growth/gelation is expected to start at $t_{\mathrm{crit}} = t_0$ in the limit that the initial number of particles $n_0 \to \infty$. As $t \uparrow t_0$, the numerical solution tends toward a self-similar solution of the form (11), with $\varphi(x) \propto x^{-\tau}$ at small x and $m_*(t)$ diverging as $(t_0 - t)^{-1/\sigma}$. The exponent τ is in general less than the analytic prediction $(\lambda + 3)/2$, and the exponent σ greater than the analytic prediction $(\lambda - 1)/2$, but they satisfy the relation $\sigma = \lambda + 1 - \tau$ for self-similar solutions of the form (11) (table 1). We studied the dependence of t_0 on the

exponents μ, ν, and λ and found that $t_0 = K/[(\lambda-1)n_0 A_{11}]$ and $K = 1$–2 if $\lambda \gtrsim 1.1$ (table 1; figure 13). At $t > t_0$, $n_k \propto k^{-(\lambda+3)/2}$ for $m_k \gg m'_*(t)$, with $m'_*(t) \to \infty$ as $t \downarrow t_0$.

For $\nu > 1$ (Section 4.4), the behaviors of the numerical solution are qualitatively similar to those found in Paper I: the numerical mass spectrum develops a power-law tail of the form $n_k \propto k^{-\nu}$ at large k that is not self-consistent, and the time at which the power-law tail develops decreases toward zero as the numerical parameter $n_{\min}$ decreases. The numerical results strongly suggest that there are no self-consistent solutions to the coagulation equation at any time and that runaway growth/gelation is instantaneous in the limit $n_0 \to \infty$. They also indicate that the time t_{crit}, in units of $1/(n_0 A_{11})$, for the onset of runaway growth decreases slowly toward zero with increasing n_0, consistent with recent Monte Carlo simulation results (Malyshkin and Goodman 2001).

The results presented in this paper and Paper I suggest several problems for future investigations. First, as we pointed out in Section 4.1, the failure to find the first correction to the leading small-x behavior $\varphi(x) \propto x^{-(1+\lambda)}$ for the orderly growth cases with $\mu > 0$ and $\lambda < 1$ in previous self-similar analysis is probably due to the unusual, damped oscillatory form of this correction. Given the information provided by the numerical results, it may now be possible to derive the first correction analytically. We suggested that the first correction could, e.g., be of the form $x^{-(1+\lambda)}f(x)\cos(B\ln x + C)$, where $f(x)$ is an increasing function of x. Second, we have found that the exponent τ for the runaway growth cases with $\nu \leq 1$ and $\lambda > 1$ is in general different from existing analytic prediction. It is important to investigate whether analytic prediction matching the numerical results could be derived. In this connection, it would be useful to obtain numerical solutions for other forms of A_{ij} and determine whether the exponent depends on the specific form of A_{ij}. Finally, it should be emphasized that rate coefficients with $\nu > 1$ do arise, and are of great interest, in astrophysics (see, e.g., Lee 1993, 2000, and references therein). For astrophysical applications, we are interested in systems with finite n_0 and interactions with the runaway particle. Thus, for $\nu > 1$, a detailed comparison of numerical solutions with finite $n_{\min}$ and Monte Carlo simulations with finite n_0 should be conducted to test the correspondence between them, and the question of whether the coagulation equation can be modified to take into account the interactions between the runaway particle and the other particles should also be investigated.

ACKNOWLEDGEMENTS

Table 1. Runaway growth cases with $\nu \leq 1$ and $\lambda > 1$.

λ	μ	ν	τ	σ	$\lambda + 1 - \tau$	$n_0 A_{11} t_0$
7/6	1/6	1	2.012	0.154	0.155	7.136
7/6	1/3	5/6	2.038	0.128	0.129	9.146
7/6	1/2	2/3	2.054	0.112	0.113	10.633
7/6	7/12	7/12	2.057	0.110	0.110	10.855
4/3	1/3	1	2.076	0.257	0.257	3.741
4/3	1/2	5/6	2.103	0.230	0.230	4.284
4/3	2/3	2/3	2.112	0.221	0.221	4.492
3/2	1/2	1	2.166	0.334	0.334	2.451
3/2	2/3	5/6	2.184	0.316	0.316	2.639
3/2	3/4	3/4	2.186	0.314	0.314	2.664
5/3	2/3	1	2.269	0.398	0.398	1.750
5/3	5/6	5/6	2.276	0.390	0.391	1.808
11/6	5/6	1	2.380	0.453	0.453	1.307
11/6	11/12	11/12	2.381	0.451	0.452	1.317
2	1	1	2.500	0.500	0.500	1.000

REFERENCES

Bak T A and Heilmann O J 1994 Post-gelation solutions to Smoluchowski's coagulation equation *J. Phys. A: Math. Gen.* **27** 4203–4209

Drake R L 1972 A general mathematical survey of the coagulation equation *Topics in Current Aerosol Research (Part 2)* ed G M Hidy and J R Brock (Oxford: Pergamon) pp 201–376

Ernst M H 1986 Kinetics of clustering in irreversible aggregation *Fractals in Physics* ed L Pietronero and E Tosatti (Amsterdam: North-Holland) pp 289–302

Ernst M H, Hendriks E M and Leyvraz F 1984 Smoluchowski's equation and the θ-exponent for branched polymers *J. Phys. A: Math. Gen.* **17** 2137–2144

Hendriks E M, Ernst M H and Ziff R M 1983 Coagulation equations with gelation *J. Stat. Phys.* **31** 519–563

Hill P J and Ng K M 1996 New discretization procedure for the agglomeration equation *AIChE J.* **42** 727–741

Jeon I 1998 Existence of gelling solutions for coagulation-fragmentation equations *Commun. Math. Phys.* **194** 541–567

Jeon I 1999 Spouge's conjecture on complete and instantaneous gelation *J. Stat. Phys.* **96** 1049–1070

Jullien R and Botet R 1987 *Aggregation and Fractal Aggregates* (Singapore: World Scientific)

Krivitsky D S 1995 Numerical solution of the Smoluchowski kinetic equation and asymptotics of the distribution function *J. Phys. A: Math. Gen.* **28** 2025–2039

Lee M H 1993 N-body evolution of dense clusters of compact stars *Astrophys. J.* **418** 147–162

Lee M H 2000 On the validity of the coagulation equation and the nature of runaway growth *Icarus* **143** 74–86

Leyvraz F and Tschudi H R 1981 Singularities in the kinetics of coagulation processes *J. Phys. A: Math. Gen.* **14** 3389–3405

Malyshkin L and Goodman J 2001 The timescale of runaway stochastic coagulation *Icarus* **150** 314–322

McLeod J B 1962 On a recurrence formula in differential equations *Quart. J. Math. Oxford* **13** 283–284

Quinlan G D and Shapiro S L 1989 Dynamical evolution of dense clusters of compact stars *Astrophys. J.* **343** 725–749

Spouge J L 1985 Monte Carlo results for random coagulation *J. Colloid Interface Sci.* **107** 38–43

Trubnikov B A 1971 Solution of the coagulation equations in the case of a bilinear coefficient of adhesion of particles *Sov. Phys. Dokl.* **16** 124–126

Tzivion S, Reisin T G and Levin Z 1999 A numerical solution of the kinetic collection equation using high spectral grid resolution: A proposed reference *J. Comput. Phys.* **148** 527–544

van Dongen P G J 1987a On the possible occurrence of instantaneous gelation in Smoluchowski's coagulation equation *J. Phys. A: Math. Gen.* **20** 1889–1904

van Dongen P G J 1987b Solutions of Smoluchowski's coagulation equation at large cluster sizes *Physica A* **145** 15–66

van Dongen P G J and Ernst M H 1985a Dynamic scaling in the kinetics of clustering *Phys. Rev. Lett.* **54** 1396–1399

van Dongen P G J and Ernst M H 1985b Comment on "Large-time behavior of the Smoluchowski equations of coagulation" *Phys. Rev. A* **32** 670–672

van Dongen P G J and Ernst M H 1985c Cluster size distribution in irreversible aggregation at large time *J. Phys. A: Math. Gen.* **18** 2779

van Dongen P G J and Ernst M H 1988 Scaling solutions of Smoluchowski's coagulation equation *J. Stat. Phys.* **50** 295–329

Wetherill G W 1990 Comparison of analytical and physical modeling of planetesimal accumulation *Icarus* **88** 336–354

Ziff R M 1980 Kinetics of polymerization *J. Stat. Phys.* **23** 241–263

Ziff R M, Ernst M H and Henriks E M 1983 Kinetics of gelation and universality *J. Phys. A: Math. Gen.* **16** 2293–2320
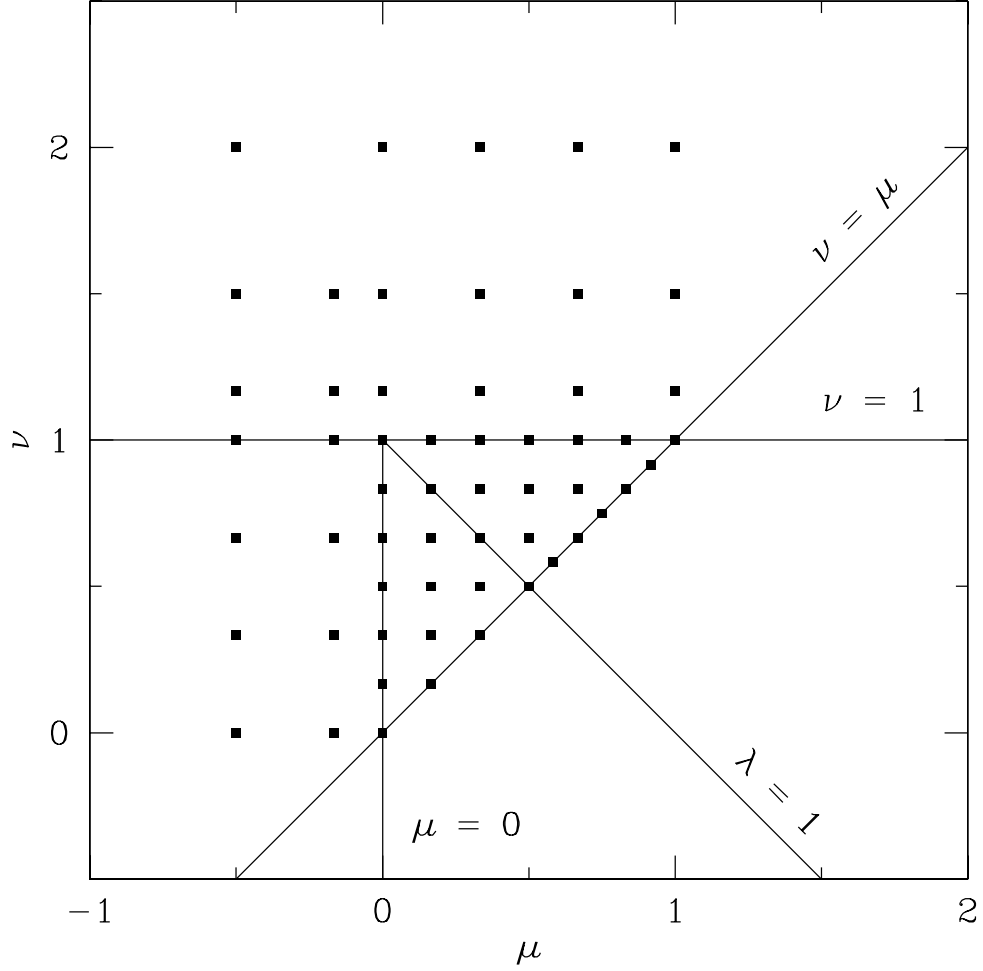
Figure 1. The exponents μ and ν of the cases for which we have obtained numerical solutions to the discrete form of the coagulation equation with rate coefficient $A_{ij} = (i^\mu j^\nu + i^\nu j^\mu)/2$. The orderly growth cases with $\nu \leq 1$ and $\lambda < 1$ and on the borderline $\nu \leq 1$ and $\lambda = 1$ are discussed in Sections 4.1 and 4.2, respectively. The runaway growth cases with $\nu \leq 1$ and $\lambda > 1$ are discussed in Section 4.3, and those with $\nu > 1$ are discussed in Section 4.4.
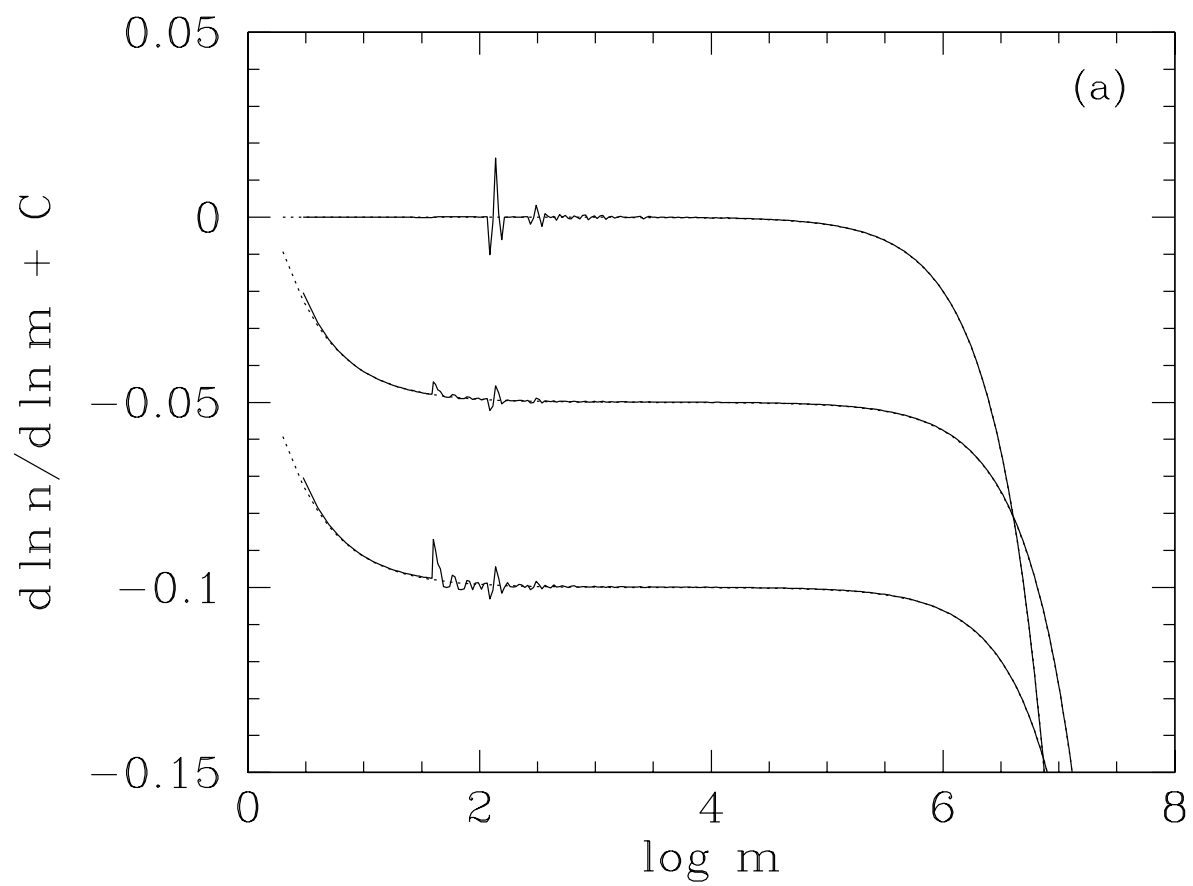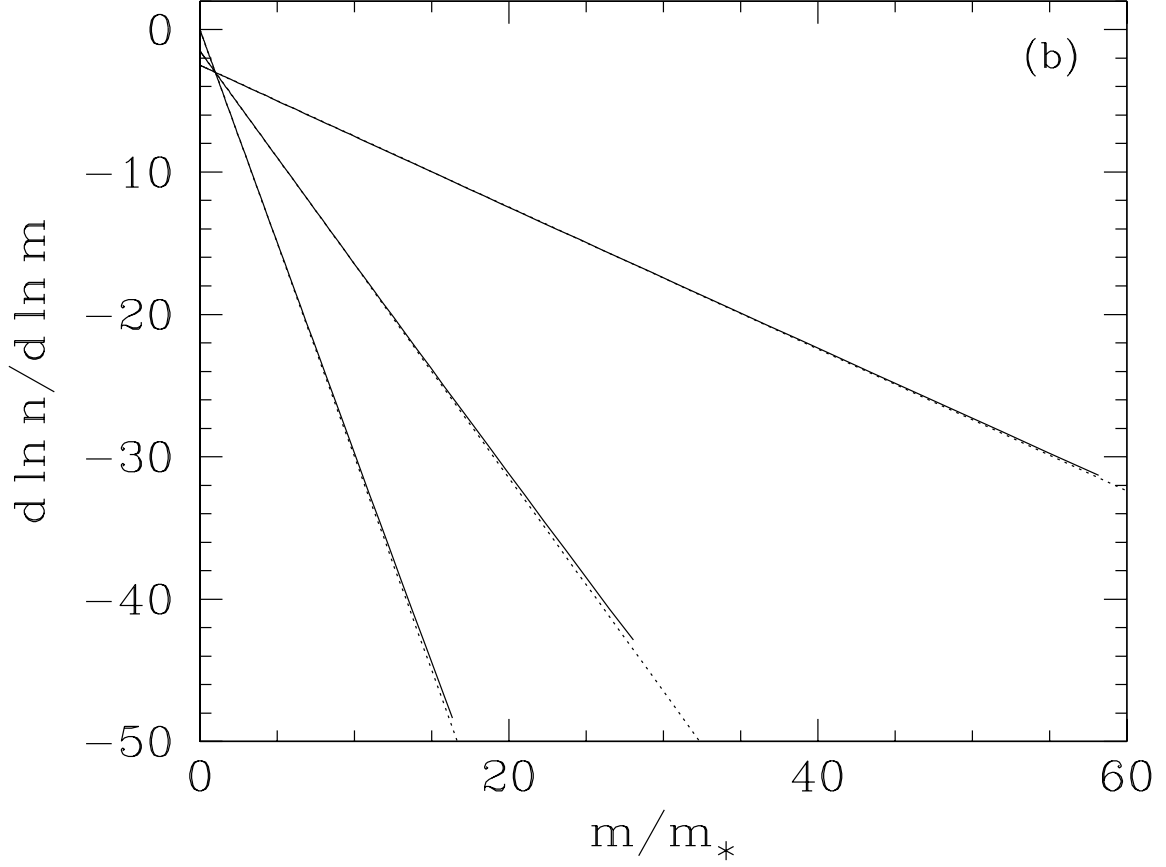
Figure 2. (a) Comparison of numerical (solid lines) and analytic (dotted lines) results for $d\ln n/d\ln m$ at $m \lesssim m_*(t)$. The lines, from top to bottom, are $d\ln n/d\ln m + C$ for $A_{ij} = 1$ at $t = 10^8$, $A_{ij} = (i + j)/2$ at $t = 18$, and $A_{ij} = ij$ at $t = 1$; the constant $C = 0$, 1.45, and 2.4, respectively. For $A_{ij} = (i + j)/2$ and ij, there is a small lag in the evolution of the numerical solutions, and the numerical results are compared to the analytic results at a slightly earlier time $(1 - \epsilon)t$, where $\epsilon = 3.5 \times 10^{-4}$ and 1.1×10^{-4}, respectively. (b) Same as (a), but at $m \gtrsim m_*(t)$. The lines, in decreasing steepness, are $d\ln n/d\ln m$ for $A_{ij} = 1$ at $t = 10^8$, $A_{ij} = (i+j)/2$ at $t = 18$, and $A_{ij} = ij$ at $t = 1$.
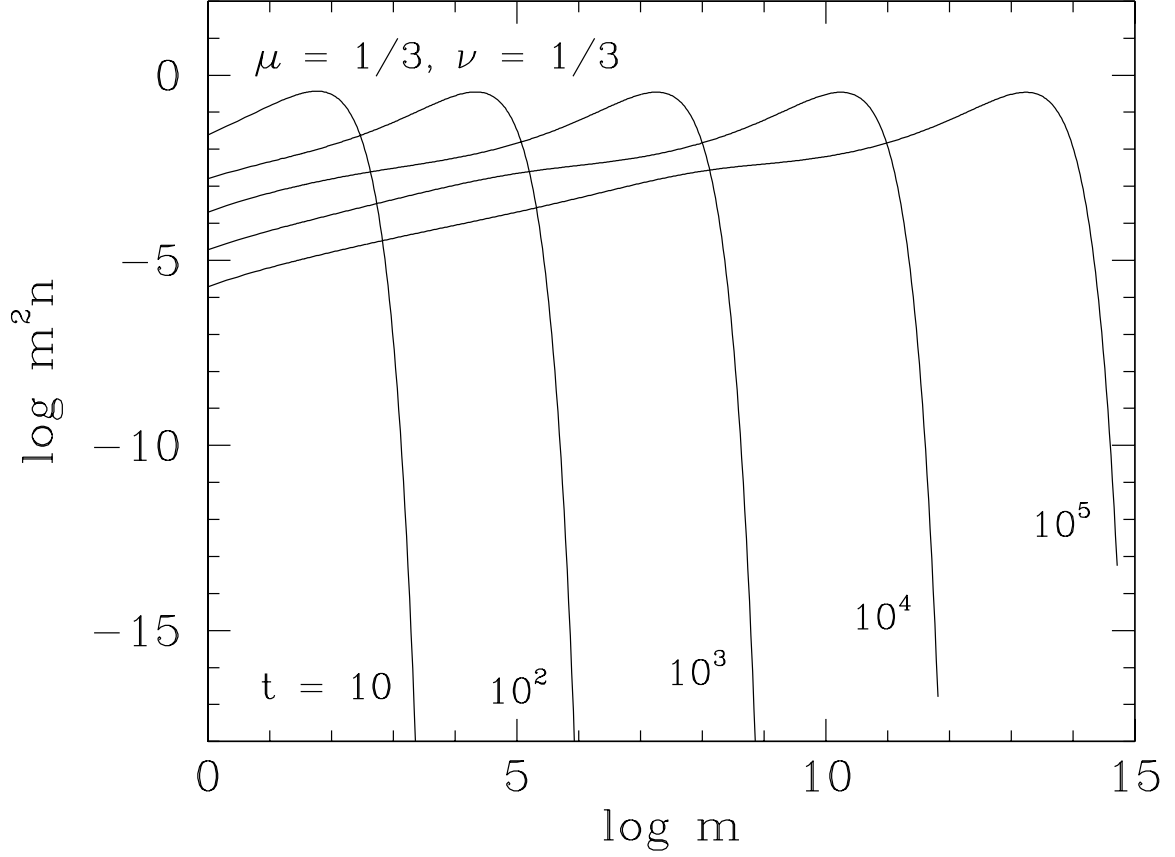
Figure 3. Evolution of the mass spectrum for $(\mu, \nu) = (1/3, 1/3)$. We plot $\log m^2 n$ as a function of $\log m$ since $m^2 n$ is the total mass per unit logarithmic mass interval: $\int m^2 n \, d \ln m = \int mn \, dm$.
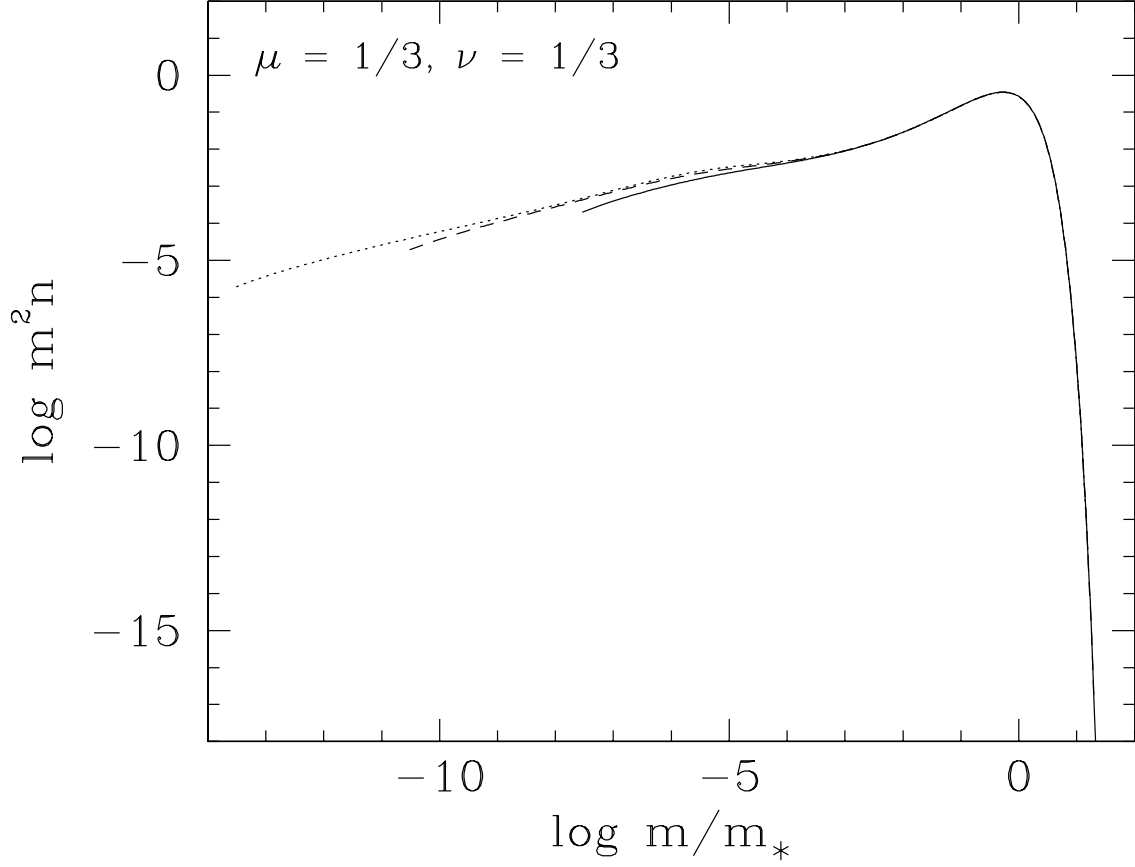
Figure 4. Approach to self-similar solution as $t \to \infty$ for $(\mu, \nu) = (1/3, 1/3)$. The numerical solution is plotted for $t = 10^3$ (solid line), 10^4 (dashed line), and 10^5 (dotted line) in the form of $\log m^2 n$ as a function of $\log m/m_*$.

(a) $\mu < 0$, $\nu \leqq 1$

(b) $\mu = 0$, $\nu \leqq 1$
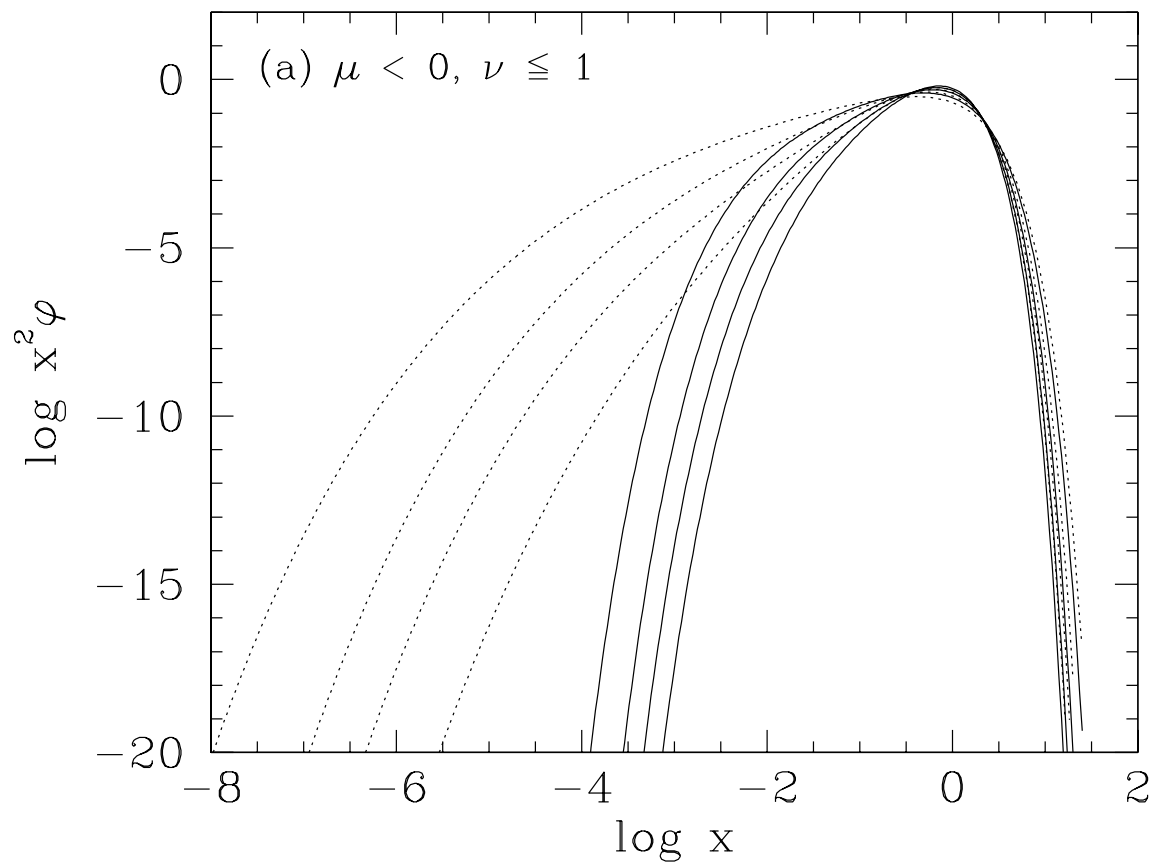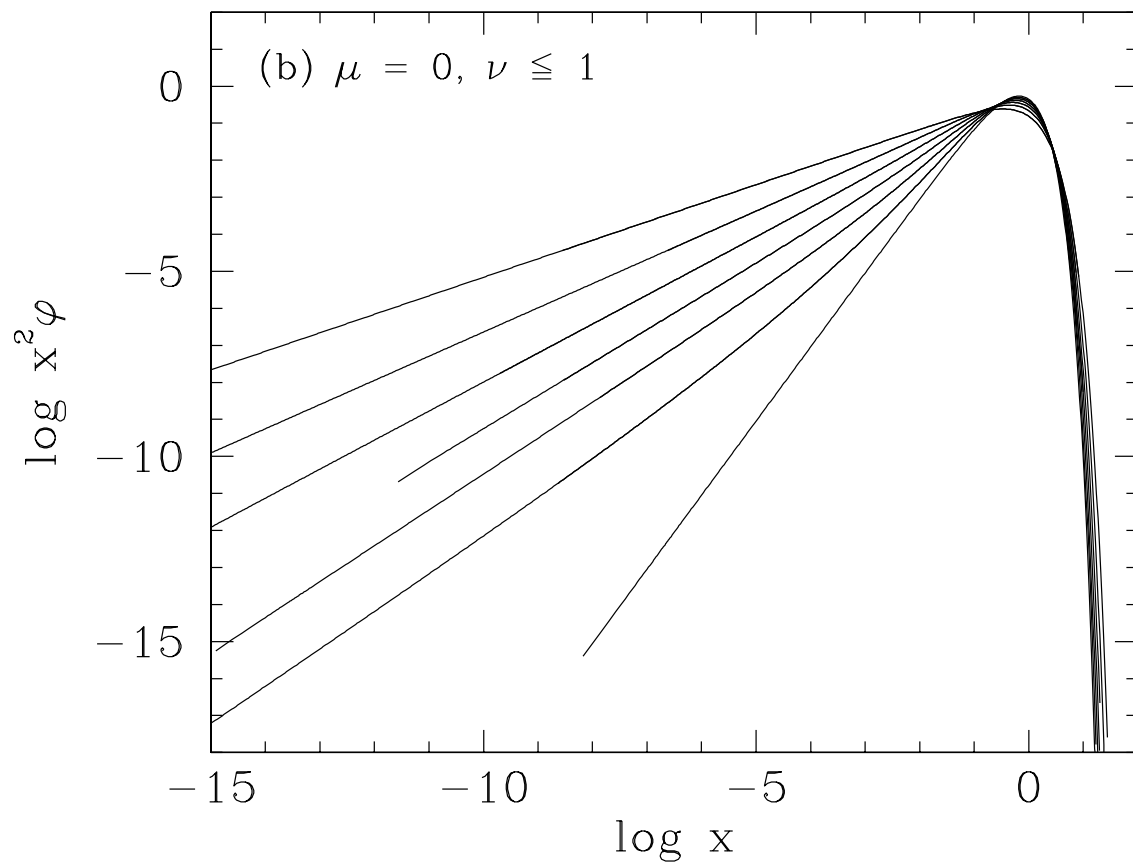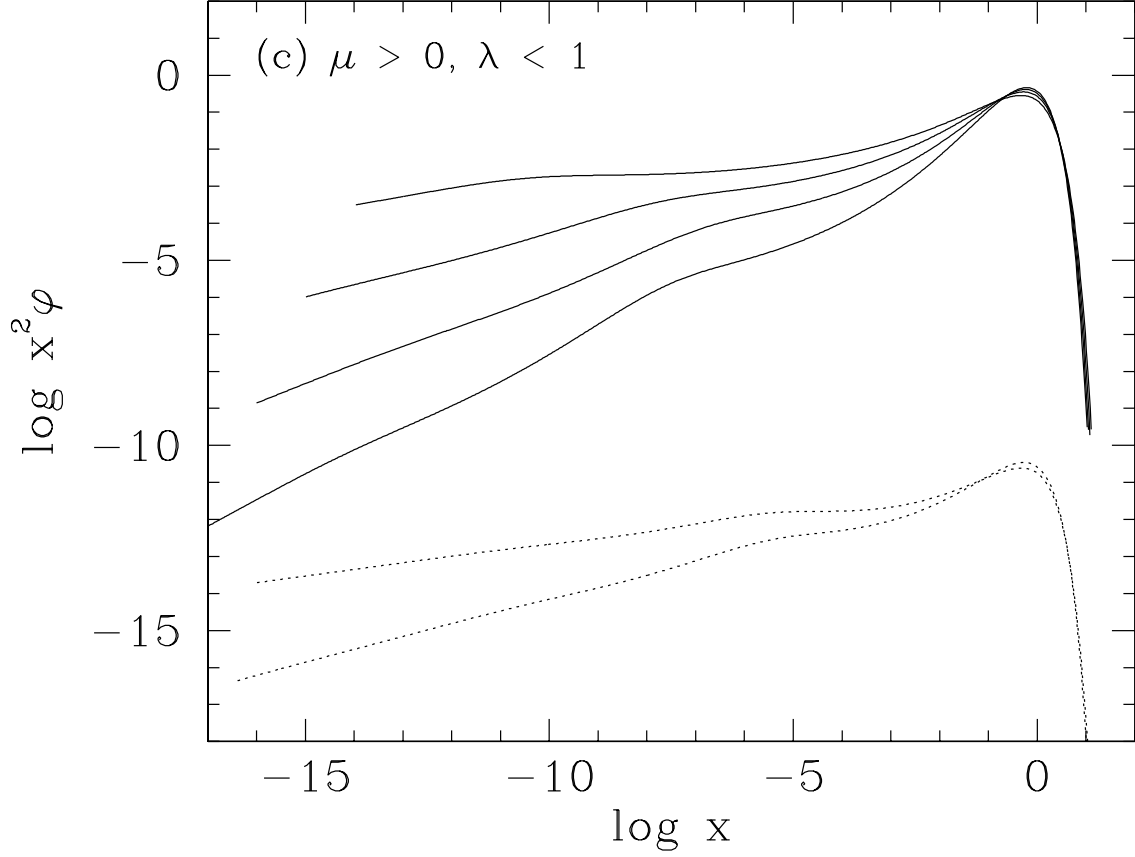
Figure 5. (a) Scaling function $\varphi(x)$ for the cases with $\mu < 0$ and $\nu \leq 1$. The solid (dotted) lines in increasing width are for $\mu = -1/2$ $(-1/6)$ and $\nu = 0, 1/3, 2/3, 1$. (b) $\varphi(x)$ for the cases with $\mu = 0$ and $\nu \leq 1$. The solid lines in increasing width are for $\nu = 0, 1/6, \ldots, 1$. (c) $\varphi(x)$ for the cases with $\mu > 0$ and $\lambda < 1$. The solid lines in increasing width are for $\mu = 1/6$ and $\nu = 1/6, 1/3, 1/2, 2/3$. The dotted lines, offset vertically by -10, are for $\mu = 1/3$ and $\nu = 1/3$ and $1/2$.
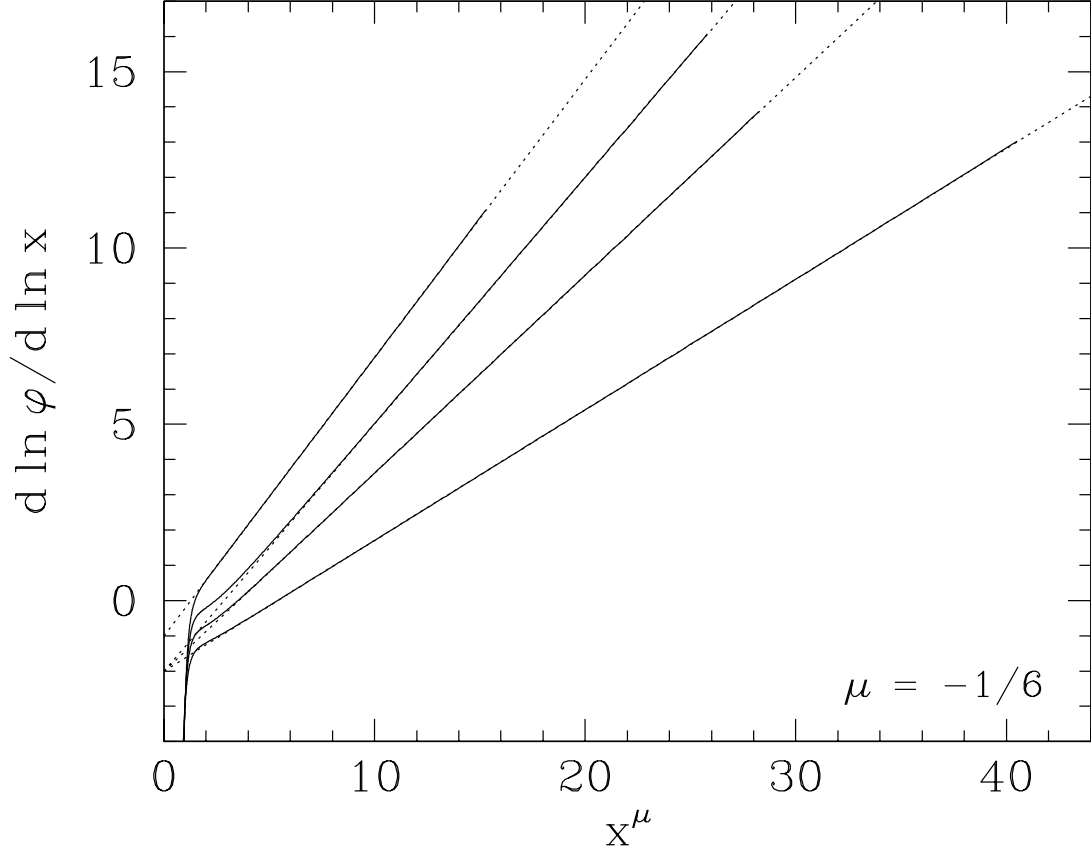
Figure 6. Logarithmic slope $d \ln \varphi / d \ln x$ as a function of x^μ for the cases with $\mu = -1/6$ and $\nu = 0, 1/3, 2/3, 1$ (solid lines from top to bottom). The dotted lines are the asymptotes approached by the numerical results at large x^μ (or small x).
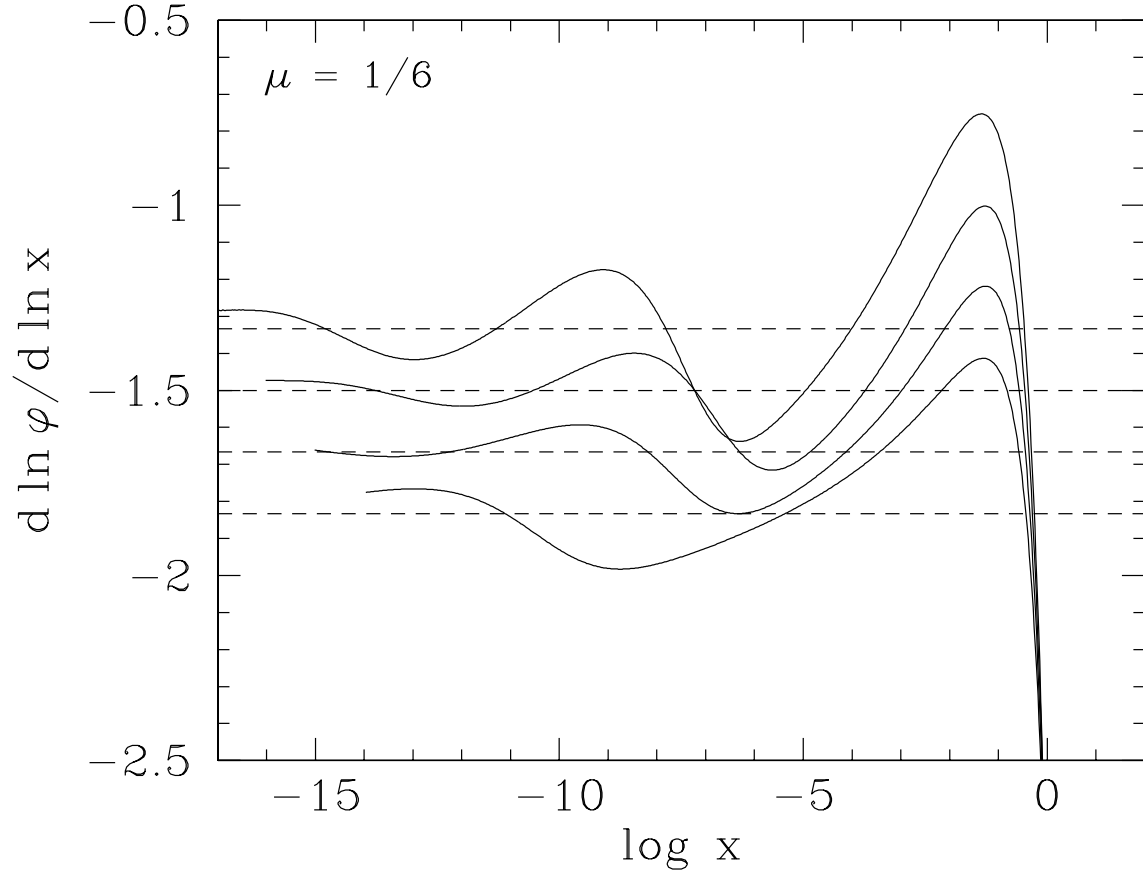
Figure 7. Logarithmic slope $d\ln\varphi/d\ln x$ for the cases with $\mu = 1/6$ and $\nu = 1/6, 1/3, 1/2, 2/3$ (solid lines from top to bottom). The dashed lines show the leading small-x behavior predicted by self-similar analysis: $d\ln\varphi/d\ln x = -(1+\lambda)$.
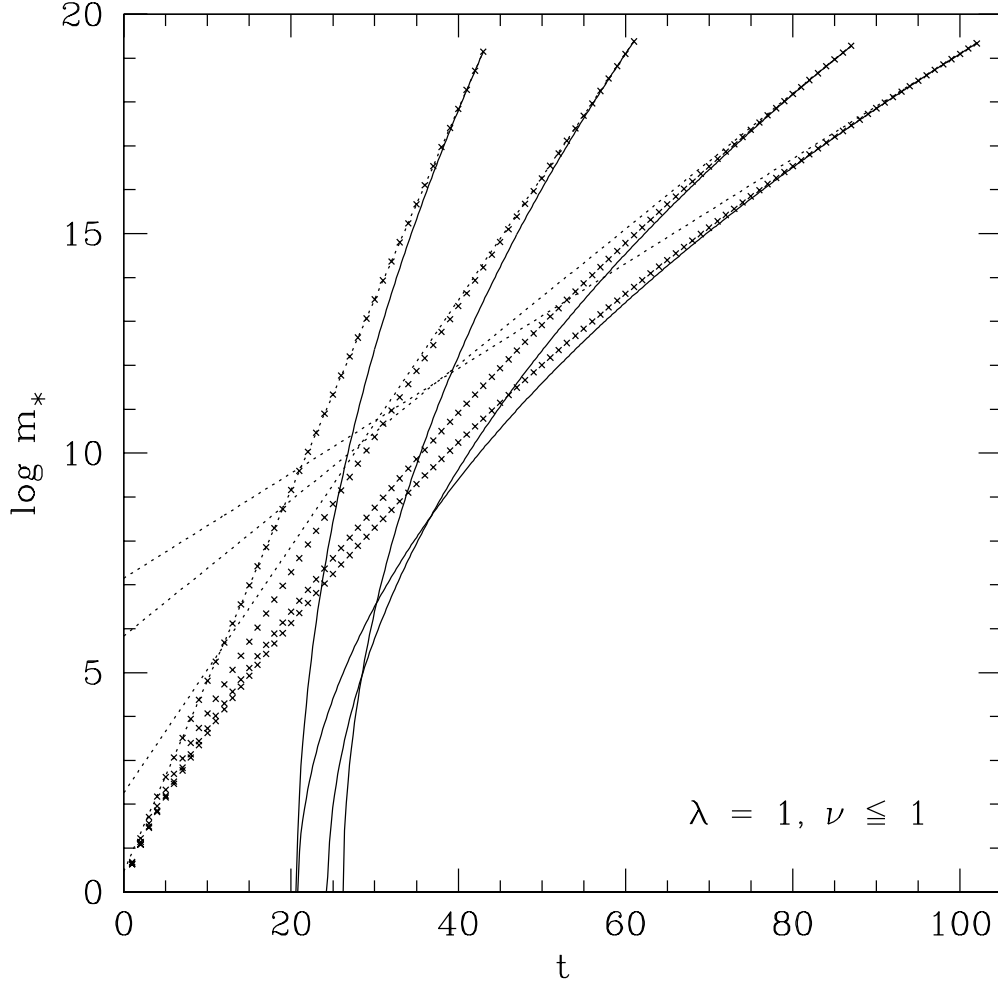
Figure 8. Characteristic mass $m_*(t)$ for the cases with $\lambda = 1$ and $\nu \leq 1$. The points, from left to right, are the numerical results for $\mu = 0, 1/6, 1/3$, and $1/2$. The dotted and solid lines show $\ln m_* = a + bt$ and $(\ln m_*)^2 = a + bt$ fitted to numerical results at the last two output times.
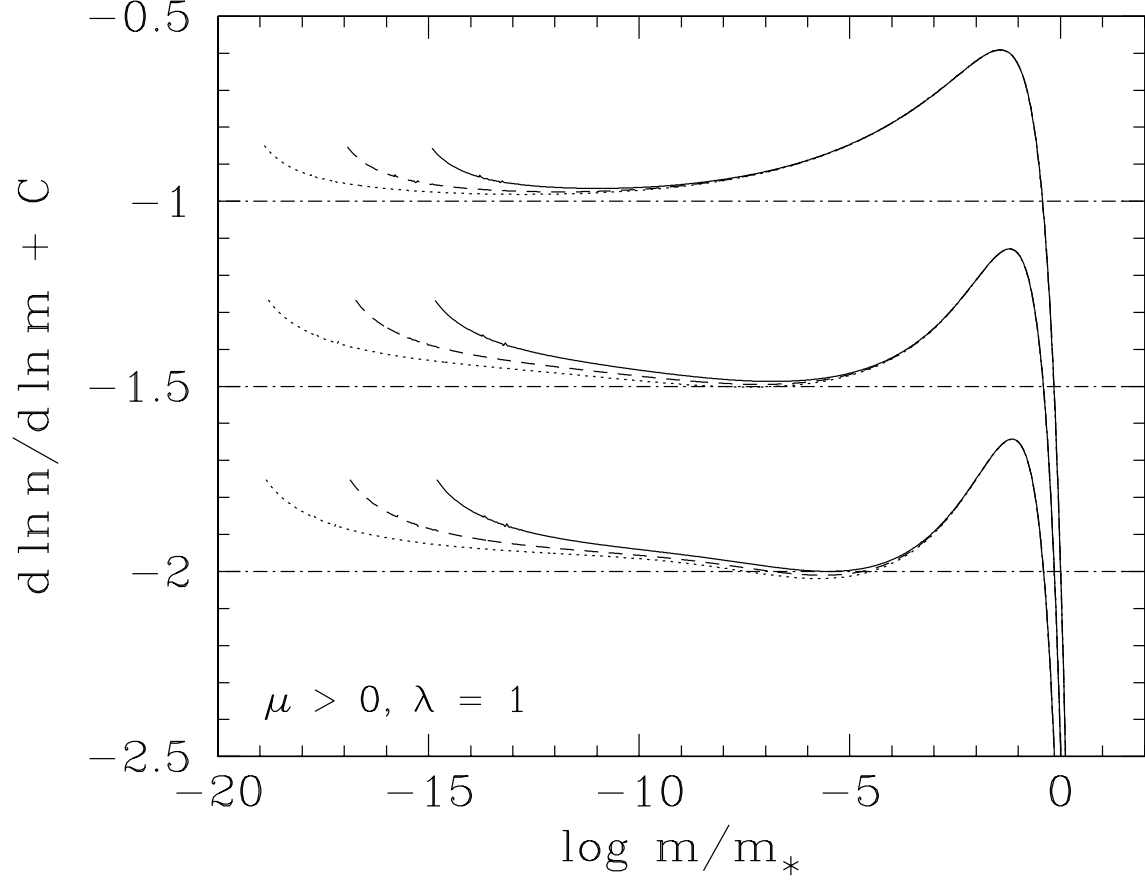
Figure 9. Logarithmic slope $d \ln n / d \ln m$ for the cases with $\mu > 0$ and $\lambda = 1$. The top lines are the numerical results for $(\mu, \nu) = (1/6, 5/6)$ at $t = 47$ (solid line), 54 (dashed line), and 61 (dotted line), offset vertically by $C = 1$. The middle lines are for $(\mu, \nu) = (1/3, 2/3)$ at $t = 63$, 74, and 87, with $C = 0.5$, and the bottom lines are for $(\mu, \nu) = (1/2, 1/2)$ at $t = 71$, 86, and 102, with $C = 0$.
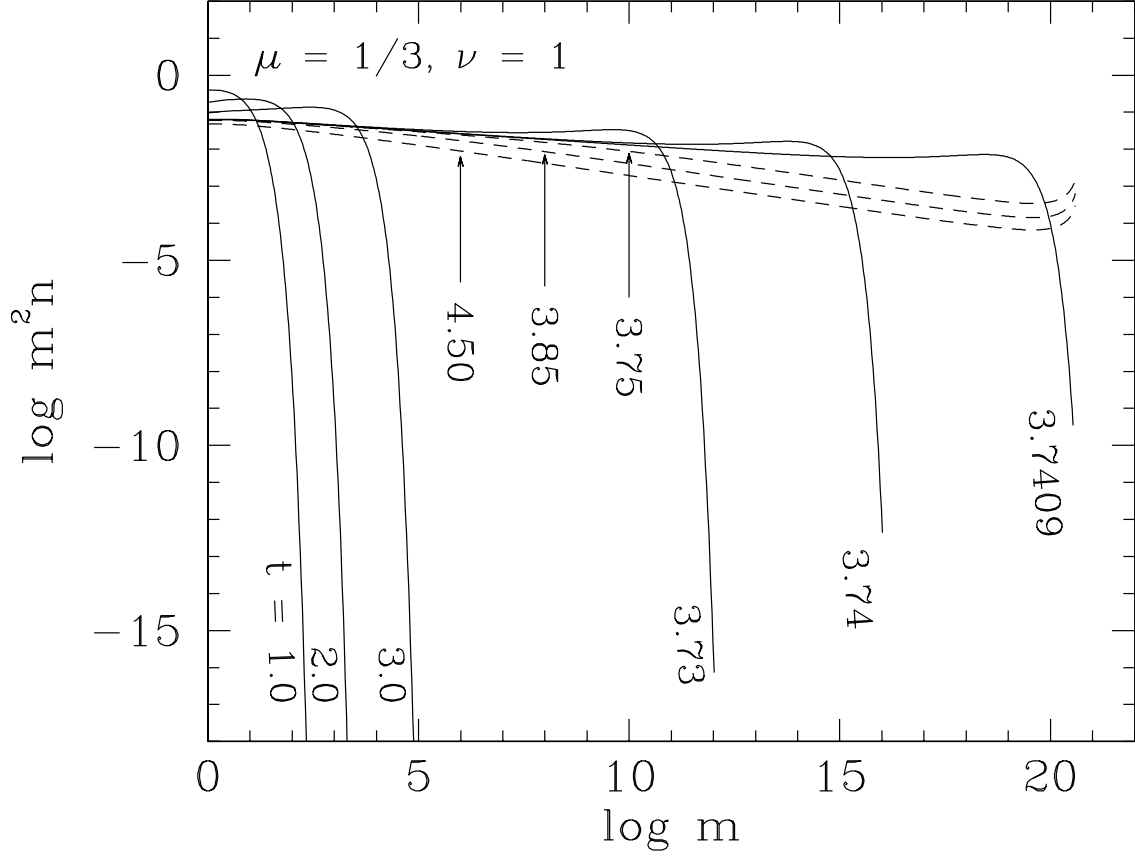
Figure 10. Evolution of the mass spectrum for $(\mu, \nu) = (1/3, 1)$ at $t \leq t_0$ (solid lines) and $t > t_0$ (dashed lines).
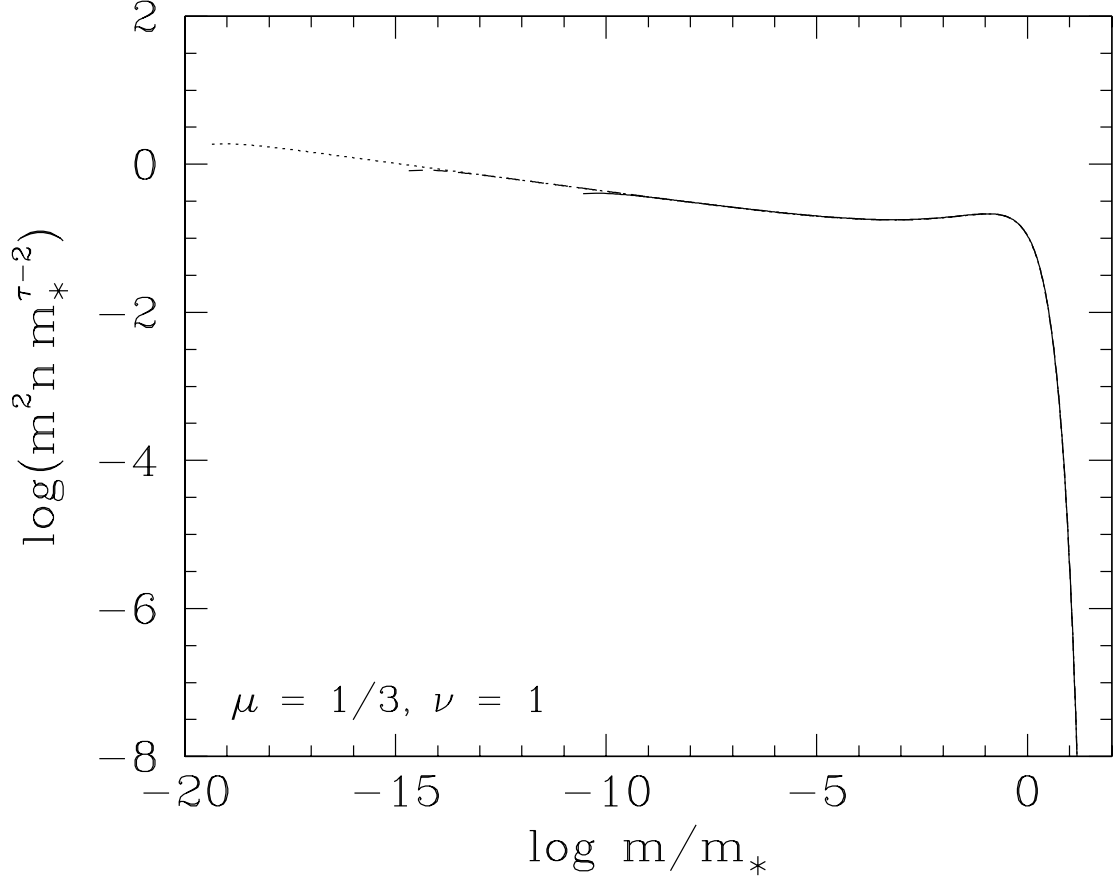
Figure 11. Approach to self-similar solution as $t \uparrow t_0$ for $(\mu, \nu) = (1/3, 1)$. The numerical solution is plotted for $t = 3.73$ (solid line), 3.74 (dashed line), and 3.7409 (dotted line) in the form of $\log(m^2 n \, m_*^{\tau-2})$ as a function of $\log m/m_*$.
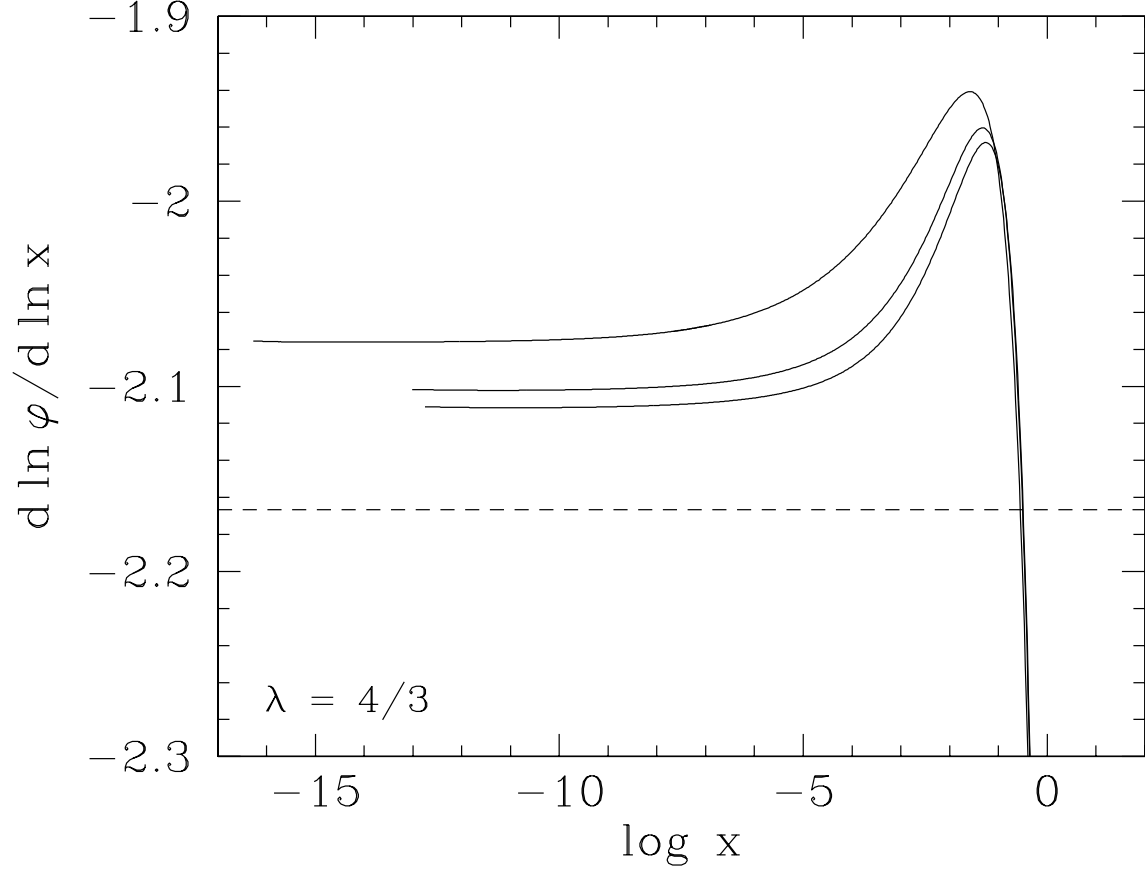
Figure 12. Logarithmic slope $d \ln \varphi / d \ln x$ for the cases with $\lambda = 4/3$. The solid lines from top to bottom are the numerical results for $(\mu, \nu) = (1/3, 1)$, $(1/2, 5/6)$, and $(2/3, 2/3)$, and the dashed line is the analytic prediction for the small-x behavior: $d \ln \varphi / d \ln x = -\tau = -(\lambda + 3)/2 = -13/6$.
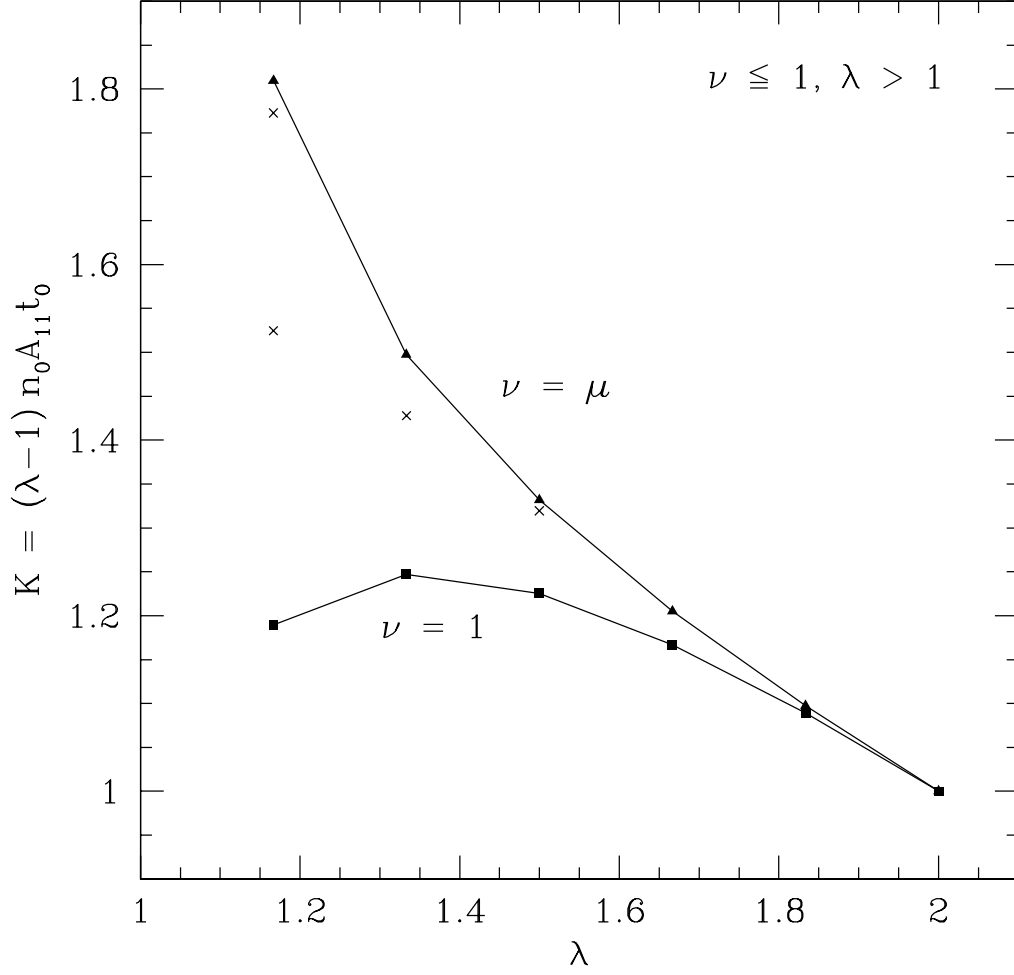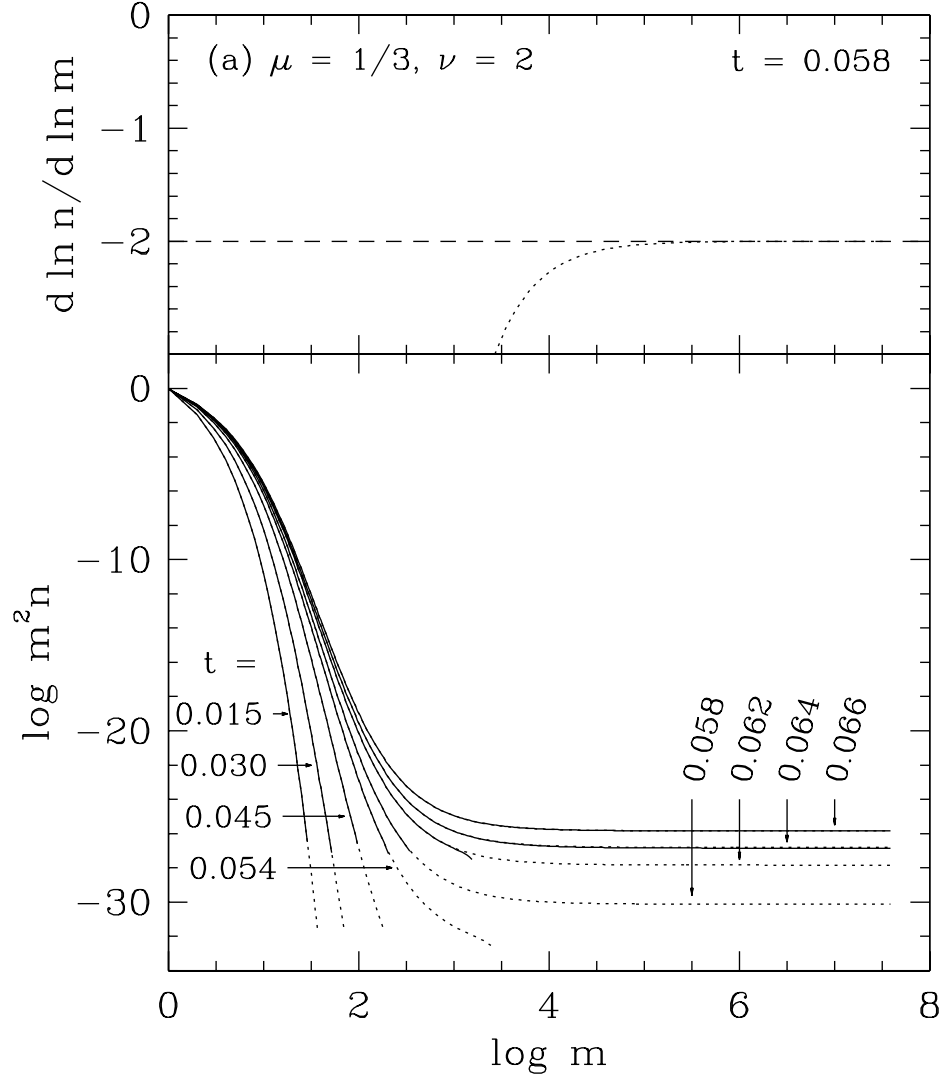
Figure 13. Parameter $K = (\lambda - 1)n_0 A_{11} t_0$ for the cases with $\nu \leq 1$ and $\lambda > 1$ listed in table 1. The cases with $\nu = 1$ and $\nu = \mu$ are represented by squares and triangles, respectively, and the remaining cases are represented by crosses.
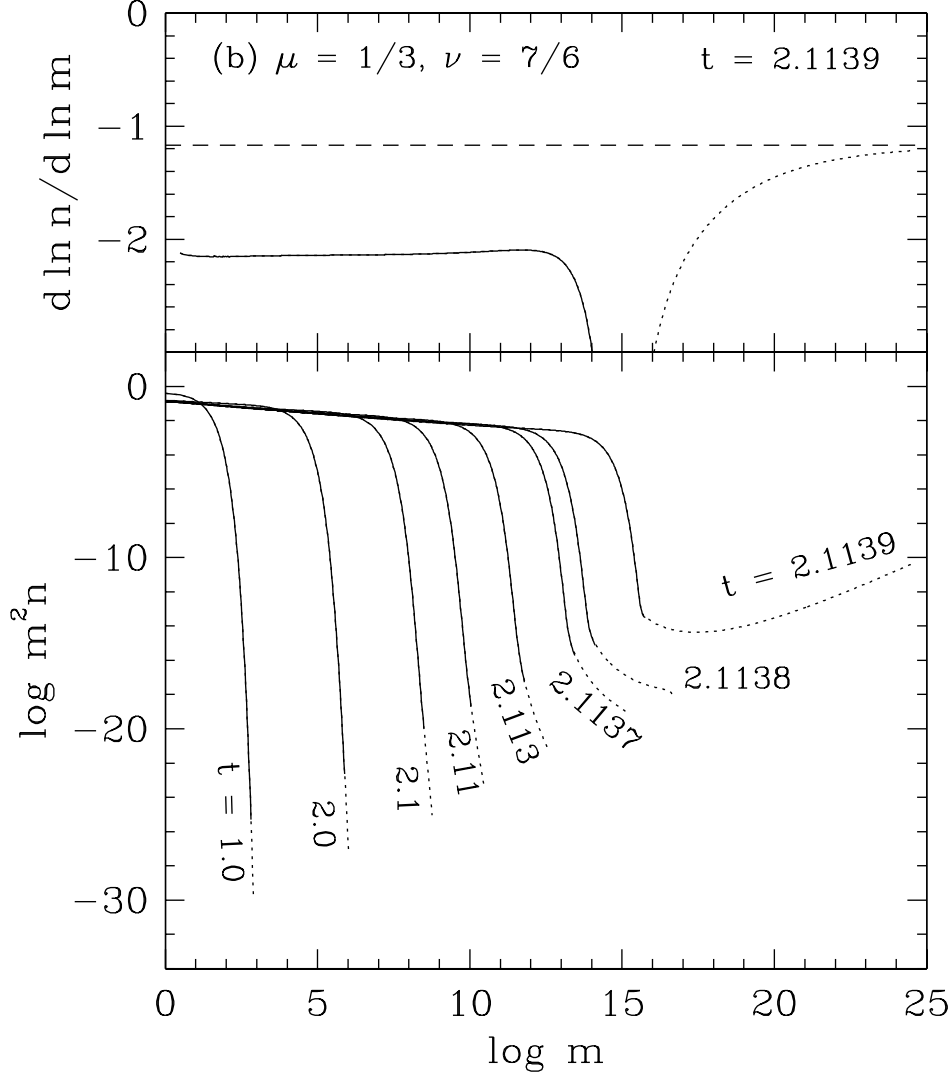
Figure 14. Evolution of the mass spectrum (*lower panels*) and logarithmic slope $d\ln n/d\ln m$ at the specified time (*upper panels*) for $\mu = 1/3$ and ν equal to (a) 2 and (b) 7/6. The numerical solutions with $n_{\min} = 10^{-30}$ (solid lines) and 10^{-35} (dotted lines) are shown. In the upper panels, the dashed lines indicate $d\ln n/d\ln m = -\nu$.